CHALMERS
UNIVERSITY OF TECHNOLOGY

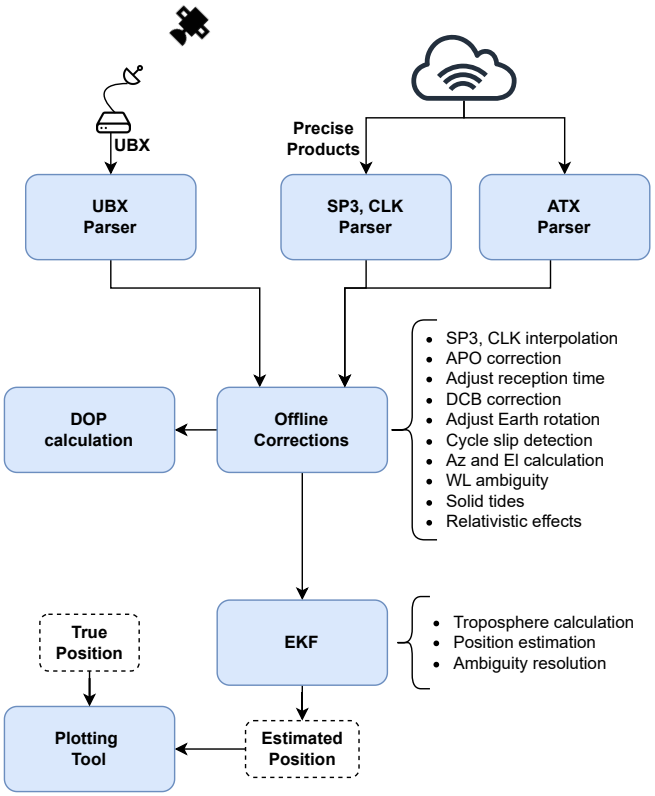

Precise Point Positioning

Multi-Constellation Ionospheric-Free Positioning Using L1/L5 Frequencies on a Low-Cost Receiver

Master's Thesis in Systems, Control and Mechatronics

Marielle Melander
Philip Pettersson

DEPARTMENT OF MECHANICS AND MARITIME SCIENCES
CHALMERS UNIVERSITY OF TECHNOLOGY
Gothenburg, Sweden 2024
www.chalmers.se

Master's Thesis in Systems, Control and Mechatronics

Precise Point Positioning

Multi-Constellation Ionospheric-Free Positioning Using L1/L5 Frequencies on a Low-Cost Receiver

Marielle Melander
Philip Pettersson

CHALMERS
UNIVERSITY OF TECHNOLOGY

Department of Mechanics and Maritime Sciences
Chalmers University of Technology
Gothenburg, Sweden 2024

Precise Point Positioning
Multi-Constellation Ionospheric-Free Positioning Using L1/L5 Frequencies on a Low-Cost Receiver
Marielle Melander
Philip Pettersson

Supervisor: Lucas Rochard, CPAC Systems AB
Examiner: Peter Forsberg, Department of Mechanics and Maritime Sciences

Master's Thesis 2024
Department of Mechanics and Maritime Sciences
Chalmers University of Technology
SE-412 96 Gothenburg
Sweden
Telephone +46 31 772 1000

Cover: Overview of implemented Precise Point Positioning solution

Typeset in LaTeX
Gothenburg, Sweden 2024

Precise Point Positioning
Multi-Constellation Ionospheric-Free Positioning Using L1/L5 Frequencies on a Low-Cost Receiver
Marielle Melander
Philip Pettersson
Department of Mechanics and Maritime Sciences
Chalmers University of Technology

Abstract

This thesis revolves around the area of satellite-based positioning using Global Navigation Satellite System (GNSS) signals from the Global Positioning System (GPS) and Galileo constellations. GNSS positioning plays a vital role in daily life, particularly in applications like navigation and timing. This project aims to develop a high-accuracy, Precise Point Positioning (PPP) solution using data from a low-cost receiver. To achieve this an ionosphere-free measurement combination based on L1 and L5 frequencies is explored instead of the conventional choice of L1 and L2. The research investigates the impact of different error sources, such as biases and atmospheric disturbances, on the accuracy of PPP. An Extended Kalman Filter (EKF)-based solution that incorporates offline corrections, cycle slip detection, and ambiguity resolution is proposed. The hardware used for data collection is the u-blox evaluation kit EKV-F9P which includes the GNSS receiver module ZED-F9P and an antenna. This low-cost dual-frequency hardware is proven to provide accurate data to implement a high-accuracy PPP solution. When enough satellites are visible, the results demonstrate a decimetre-level accuracy for stationary positioning estimation. However, due to the limited availability of L5 frequency signals, continuous precise positioning is not always possible. Despite this limitation, the work contributes to advancing GNSS positioning technology and lays the groundwork for future enhancements in PPP-based applications.

Keywords: PPP, GNSS, EKF, dual-frequency, Ionosphere-free, low-cost, EVK-F9P, u-blox

Acknowledgements

We would like to extend our gratitude to our examiner, Peter Forsberg, and our supervisor, Lucas Rochard, for their support and feedback during our thesis project. We also want to thank CPAC Systems AB for providing the opportunity and facilities to perform this master's thesis.

Marielle Melander, Philip Pettersson, Gothenburg, June 2024

Supervisor: Lucas Rochard, CPAC Systems AB
Examiner: Peter Forsberg, Department of Mechanics and Maritime Sciences

List of Acronyms

Below is the list of acronyms that have been used throughout this thesis listed in alphabetical order:

APC	Antenna Phase Centre
APO	Antenna Phase Offset
BDS	BeiDou Navigation Satellite System
CDDIS	Crustal Dynamics Data Information System
CPA	Carrier Phase Ambiguity
DCB	Differential Code Biases
DGNSS	Differential GNSS
DOP	Dilution Of Precision
DOY	Day Of Year
ECEF	Earth-centred Earth-Fixed
EKF	Extended Kalman Filter
ENU	East, North, Up
GF	Geometry-Free
GLONASS	Global Navigation Satellite System
GNSS	Global Navigation Satellite Systems
GPS	Global Positioning System
HDOP	Horizontal Dilution Of Precision
IEEE	Institute of Electrical and Electronics Engineers
IF	Ionosphere-Free
IERS	International Earth Rotation and Reference System Service
ITRF	International Terrestrial Reference Frame
LAMBDA	Least-Squares Ambiguity Decorrelation
LOS	Line of Sight
MLAMBDA	Modified LAMBDA
MW	Melbourne-Wübbena
NavIC	Navigation with Indian Constalletion
NL	Narrow-Lane
NTRIP	The Networked Transport of RTCM via Internet Protocol
PPP	Precise Point Positioning
PPP-AR	Ambiguity-Resolution PPP
PRN	Pseudo-Random Noise
QZSS	Quasi-Zenith Satellite System
RF	Radio Frequency
RTK	Real-Time Kinematic

SD	Single Difference
SNR	Signal-To-Noise Ratio
SSR	State Space Representation
TEC	Total Electron Content
TRS	Terrestrial Reference System
VDOP	Vertical Dilution Of Precision
WARKT	Wide Area RTK
WL	Wide-Lane
ZHD	Zenith Hydrostatic Delay
ZWD	Zenith Wet Delay

Nomenclature

Below is the nomenclature of indices, parameters, and variables that have been used throughout this thesis.

Indices

s	Index for satellite
r	Index for receiver
j	Index for band

Constants

c: $299,792,458$	Speed of light in vacuum (light celerity) [m/s]
h_2: 0.6078	Nominal degree 2 Love number
l_2: 0.0847	Nominal degree 2 Shida number
GM_E: $3.986004418 \cdot 10^{14}$	Earth's gravitational parameter [m^3/s^2]
GM_2: $4.9048695 \cdot 10^{12}$	Moon's gravitational parameter [m^3/s^2]
GM_3: $1.32712440018 \cdot 10^{20}$	Sun's gravitational parameter [m^3/s^2]

Variables

f	Frequency [Hz]
λ	Wavelength [m]
ρ	Geometric distance [m]
P	Pseudorange [m]
I	Ionospheric delay [m]
T	Tropospheric delay [m]
L	Carrier phase measurement [Cycles]
Φ	Carrier phase measurement [m]

N	Integer Carrier phase ambiguity [Cycles]
δb	Code hardware bias [m]
δB	Phase hardware bias [m]
w	Carrier phase windup effect [Cycles]
dt	Clock errors [m]
$\mathbf{r}$	Position in ECEF [m]
$\mathbf{v}$	Velocity in ECEF [m]
Δt_{tp}	Signal travel time using pseudorange [s]
Δt_{tg}	Signal travel time using geometric distance [s]
az	Azimuth angle to the satellite from the receiver [deg]
el	Elevation angle to the satellite from the receiver [deg]
Δ_{rel}	Special relativistic effect [m]
ω_e	Earth's rotation speed [m/s]
$DCB^s_{i,j}$	Differential Code Bias between band i and j for satellite s
$DPB^s_{i,j}$	Differential Phase Bias between band i and j for satellite s

Contents

List of Figures

List of Tables

1

Introduction

Global Navigation Satellite Systems (GNSS) have become an indispensable part of modern life, providing accurate location information for a myriad of applications ranging from navigation and mapping to timing and synchronization. The backbone of GNSS systems includes satellite constellations such as the U.S. Global Positioning System (GPS), the Russian Federation Global Navigation Satellite System (GLONASS), the European Galileo system, and the Chinese BeiDou Navigation Satellite System (BDS) [3]. These systems are mostly global, meaning they provide coverage on large parts of the Earth, in contrast to the Japanese system Quasi-Zenith Satellite System (QZSS) and India's Navigation with Indian Constellation (NavIC), which are regional systems.

At least four satellites are required to determine the receiver position, in X, Y and Z directions, and the receiver clock bias. If more variables are to be determined, more satellites are needed to accurately estimate the position and by using multiple constellations, the number of available satellites increases [4]. This process is called multi-GNSS. The satellites transmit signals containing various data to receivers on the ground, which can be used to determine the receiver's location. Calculations are performed to extract the distance to each satellite and, through trilateration, the position of the receiver. During the transmission from satellite to receiver, the signals are affected by many disturbances, which affect the accuracy of the estimated receiver position. Some of these error sources and corresponding solutions will be discussed in the following sections.

There are relative and precise positioning methods, with the difference being how many receivers are needed in order to estimate the position accurately. The relative positioning depends on two or more receivers, one or more stationary base stations and one mobile rover. The rover position is estimated using complementary data transmitted by the base station. This method can produce centimetre-level positioning accuracy but is limited by the range between the two receivers [5]. On the other hand, precise positioning only uses one receiver but has a longer convergence time, i.e., the time it takes until an estimate is calculated. This can be problematic for demanding systems such as automated vehicles [4]. This work will aim to develop and implement a precise point positioning (PPP) method, where a deep understanding of multiple error sources is needed.

The next Chapter, 2, contains theory regarding the GNSS signals and their contents, relevant error sources and how to evaluate GNSS positioning. In Chapter 3, relevant literature is presented along with techniques to mitigate error sources and how to solve the carrier phase ambiguities. The methodology of the project is also described. Chapter 4 includes the results, which are then discussed in Chapter 5 and the conclusions are

presented in Chapter 6.

1.1 Research questions

- How can the hardware components of a multi-constellation GNSS receiver be optimized for cost-effectiveness without compromising accuracy?
- What strategies can be implemented to mitigate common sources of error in multi-constellation GNSS positioning, particularly in low-cost solutions, to enhance overall accuracy?
- How does the developed GNSS solution compare in terms of accuracy, reliability, and performance against both proprietary and open-source alternatives under various environmental conditions?

1.2 Methodology

As the research questions describe, this project aims to develop a low-cost GNSS solution by combining techniques for mitigating error sources such as biases and atmospheric disturbances.

To achieve this goal, a comprehensive literature study will be performed to gather information regarding GNSS theory. The focus will be on deepening the knowledge of the possible sources of errors for absolute positioning systems and what corrections must be performed to achieve high accuracy. Time will be spent delving into the area of PPP by going through similar implementations and finding areas of development that can be improved in this thesis.

Research on available hardware will be conducted to find a receiver that can collect raw data, which will be used to test the implementation. The receiver also has to be able to receive two frequencies while still being a low-cost device.

1.3 Limitations / Demarcations

The limitations of this thesis include how the data is collected and handled and what constellations will be used. To validate and test the implementation, GNSS data have to be used. Only data collected by the chosen hardware will be used. A stationary receiver will acquire this data, meaning the implementation will be a static positioning solution. Additionally, all the calculations for the corrections and the position estimation will be performed in post-processing, not in real-time. The project will utilise a dual-constellation implementation, using data from GPS and Galileo satellites.

2

Theory

This section initially provides a general overview of GNSS positioning and explains the steps required to determine a receiver's position. Then, it delves into the GNSS signals and observables, along with various coordinate systems relevant to GNSS positioning. The section also discusses common sources of error and how to manage them. Finally, it presents different methods of positioning (relative and absolute) and explains how to evaluate the accuracy of the estimations provided by these methods.

2.1 GNSS signals

This section describes the structure of a GNSS signal and its three main components, the carrier wave, the ranging code and the navigation data.

2.1.1 Radio Frequency (RF) Carrier

The satellite transmitter produces a sinusoidal wave with a constant frequency called the radio frequency carrier or carrier wave [3]. The carrier wave frequency ranges from 1 to 2GHz, depending on the constellation. The Institute of Electrical and Electronics Engineers (IEEE) has defined a letter band designation to categorize ranges of frequencies for specific purposes [6], as shown in table 2.1. The GNSS signals' carrier wave frequencies fall within the L-band range.

Table 2.1: Radar-frequency letter bands.

Band designation	Nominal frequency range
HF	3 MHz to 30 MHz
VHF	30 MHz to 300 MHz
UHF	300 MHz to 1000 MHz
L	1 GHz to 2 GHz
S	2 GHz to 4 GHz
C	4 GHz to 8 GHz
X	8 GHz to 12 GHz
K_u	12 GHz to 18 GHz
K	18 GHz to 27 GHz
K_a	27 GHz to 40 GHz
V	40 GHz to 75 GHz
W	75 GHz to 110 GHz

The L-band is divided into three main frequencies for transmitting GPS signals: L1 (1575 MHz), L2 (1227 MHz), and L5 (1176 MHz). For the Galileo constellation, the main frequencies are E1 (1575 MHz), E5a (1176 MHz) and E5b (1207 MHz). The frequencies of E1 and E5a correspond to those of L1 and L5 of the GPS signal and will henceforth be referred to as L1 and L5.

Each of these signals has unique characteristics. For instance, [7] states that L1 has the lowest ionospheric refraction error, L2 performs best in cross-correlation, and L5 has the highest power. Further, the L5 signal is described as ideal for high-precision positioning and is designed for safety-of-life applications due to its high power. It is also mentioned that L5 has a lower standard deviation when estimating position.

The radio frequency carrier alone does not provide any information, but adding data with modulation is possible. Modulation is the process of adding information to a carrier wave by converting the data, in the form of symbols, to a carrier waveform [8]. An example of this operation is depicted in Figure 2.1. The figure includes the carrier wave, a code signal, or ranging code, and the resulting signal when modulating the two. The ranging code is explained in the next section.

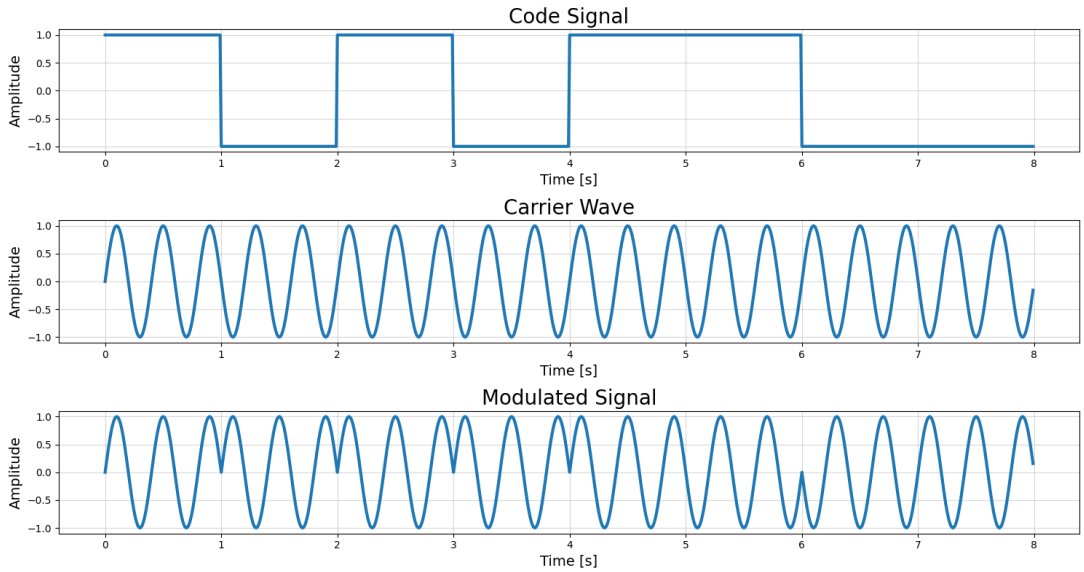

Figure 2.1: Ranging code, carrier wave and the modulated signal.

2.1.2 Pseudo-Random Noise (PRN) ranging codes

Ranging codes consist of binary sequences that enable the receiver to calculate the signal's travel time from the satellite to the receiver [4]. GNSS ranging codes, that are modulated onto the carrier, are referred to as pseudo-random as they do not have an apparent pattern. However, they repeat after a certain duration [9].

2.1.3 Navigation data

The navigation data contains information such as the satellite ephemeris, atomic clock data, corrections and the almanac data [4]. The satellite ephemeris consists of the necessary parameters to calculate the position of the satellite at a given point in time, and the almanac consists of information about all the satellites in a constellation including health status and rough orbit information [4]. This message is crucial for determining the receiver's location by providing vital information about the satellites.

2.2 GNSS Observables

GNSS observables are the measurements a receiver computes from the signals it receives from a satellite. There are two main types of observables, the pseudorange and the carrier phase.

2.2.1 Pseudorange

The pseudorange, also referred to as code phase ranging or code measurement, is the distance between a satellite and receiver calculated using the signal travel time retrieved from the ranging code signal. If no disturbances or errors are present, the pseudorange is equal to the geometric distance ρ (actual distance) described in Equation (2.1) for satellite s and receiver r [10].

$$\rho_r^s = c(t_r - t^s) = c\Delta t = \sqrt{(x^s - x_r)^2 + (y^s - y_r)^2 + (z^s - z_r)^2} \tag{2.1}$$

Where

- c is the speed of light in vacuum
- t_r is the time when the signal is received at the receiver
- t^s is the time when the signal is transmitted from the satellite
- Δt is the transmission time of the signal.

Since there are errors and disturbances within practical scenarios, the pseudorange is not equal to the geometric distance and can be written as in Equation (2.2) for the band j.

$$\begin{aligned} P_j^s &= c\left(\bar{t}_r - \bar{t}^s\right) \\ \bar{t}_r &= t_r + dt_r \\ \bar{t}^s &= t^s + dt^s \end{aligned} \tag{2.2}$$

Where

- P_j^s is the pseudorange observable
- dt_r is the receiver clock bias
- dt^s is the satellite clock bias.

Equation (2.2) can be further developed by introducing the geometric distance and the most prominent disturbances as described in Equation (2.3) [4].

$$P_j^s = \rho_r^s + c\,(dt_r - dt^s) + \Delta_{rel} + b_r - b_j^s + T^s - g_j I + \varepsilon(P_j^s) \tag{2.3}$$

Where

- ρ_r^s is the geometric (true) distance from the antenna phase centre (APC) of the satellite to the APC of the receiver
- Δ_{rel} is the special relativistic effect
- b_r is the code receiver instrumental delay
- b_j^s is the code satellite instrumental delay
- T^s is the tropospheric delay
- I is the ionospheric delay
- g_j is the frequency-specific factor that affects the ionospheric delay
- $\varepsilon(P_j^s)$ is the residual term that denotes the unmodeled terms.

2.2.2 Carrier Phase Measurement

The carrier phase measurement measures the beat frequency, which is the difference in frequency between the signal generated by the receiver's oscillator and the signal transmitted from the satellite [11]. The beat frequency technique is utilized to produce an ambiguous measurement of the distance to the satellite in cycles, offset by an ambiguous number of whole wavelengths. In contrast to the pseudorange method, the carrier phase measurement is less influenced by noise and can theoretically provide accuracy within a couple of millimetres [11]. The carrier phase measurement is written in Equation (2.5) in the same manner as the pseudorange measurement.

$$\lambda_j L_j^s = \Phi_j^s \tag{2.4}$$

$$\Phi_j^s = \rho_r^s + c(dt_r - dt^s) + \Delta_{rel} + B_r - B_j^s + T^s - g_j I + \lambda_j(N_j^s + w^s) + \varepsilon(\Phi_j^s) \tag{2.5}$$

Where

- L_j^s is the carrier phase measurement in cycles
- λ_j is the wavelength of the signal
- Φ_j^s is the carrier phase measurement in meters
- B_r is the code receiver instrumental delay
- B_j^s is the code satellite instrumental delay
- w is the carrier phase windup effect
- N_j^s is the integer ambiguity.

When the receiver locks on to the signal, it can only determine the signal's phase shift and frequency change and not the number of whole cycles between the satellite and receiver, resulting in a carrier phase ambiguity (CPA) that needs to be estimated in order to use the carrier phase measurement [12].

2.2.3 Combination of signals

When combining GNSS observables from different frequencies of the same satellite, new measurements with updated characteristics can be computed. The following combinations use pairs of signals, i.e., dual-frequency measurements.

2.2.3.1 Ionosphere-free (IF)

The IF measurements are calculated according to Equations (2.6) and (2.7) [4].

$$\boldsymbol{\Phi}_{IF} = \frac{f_1^2 \boldsymbol{\Phi}_1 - f_5^2 \boldsymbol{\Phi}_5}{f_1^2 - f_5^2} \tag{2.6}$$

$$\boldsymbol{P}_{IF} = \frac{f_1^2 \boldsymbol{P}_1 - f_5^2 \boldsymbol{P}_5}{f_1^2 - f_5^2} \tag{2.7}$$

This combination is free from up to 99.9% of the ionospheric disturbance [4]. The measurement obtained from the IF combination has a higher level of noise compared to the individual signals [13]. The noise will be amplified with a scale factor that is dependent on the squared wavelength ratios $\mu_j = \lambda_j^2/\lambda_1^2$, for band j [14]. The scale factor is calculated using Equation (2.8).

$$\sqrt{\frac{\mu_1^2 + \mu_5^2}{(\mu_5 - \mu_1)^2}} \approx 2.59 \tag{2.8}$$

2.2.3.2 Geometry-free (GF)

As the name suggests, the GF combination is free from the geometric parts of the measurement, such as the clocks and non-frequency dependent effects [4]. The combined

measurements are described by Equations (2.9) and (2.10).

$$\boldsymbol{\Phi}_{GF} = \boldsymbol{\Phi}_1 - \boldsymbol{\Phi}_5 \tag{2.9}$$
$$\boldsymbol{P}_{GF} = \boldsymbol{P}_5 - \boldsymbol{P}_1 \tag{2.10}$$

2.2.3.3 Narrow-lane (NL)

Using Equations (2.11) and (2.12) NL measurements are calculated that have a particularly short wavelength and less noise [4].

$$\boldsymbol{\Phi}_{NL} = \frac{f_1\boldsymbol{\Phi}_1 + f_5\boldsymbol{\Phi}_5}{f_1 + f_5} \tag{2.11}$$
$$\boldsymbol{P}_{NL} = \frac{f_1\boldsymbol{P}_1 + f_5\boldsymbol{P}_5}{f_1 + f_5} \tag{2.12}$$

2.2.3.4 Wide-lane (WL)

Unlike the NL combination, the WL measurement has an especially large wavelength, which is useful for ambiguity resolution [4]. The calculation of the WL combination is shown in Equations (2.13) and (2.14).

$$\boldsymbol{\Phi}_{WL} = \frac{f_1\boldsymbol{\Phi}_1 - f_5\boldsymbol{\Phi}_5}{f_1 - f_5} \tag{2.13}$$
$$\boldsymbol{P}_{WL} = \frac{f_1\boldsymbol{P}_1 - f_5\boldsymbol{P}_5}{f_1 - f_5} \tag{2.14}$$

2.2.3.5 Melbourne-Wübbena (MW)

The ionospheric dependence can be removed from the $\boldsymbol{\Phi}_{WL}$ and $\boldsymbol{P}_{NL}$ measurements by combining them according to the MW combination, which is calculated with Equation (2.15). Further benefits with this combination include a longer wavelength than the original measurements due to the WL measurement and reduced measurement noise thanks to the NL measurement [4].

$$MW = \boldsymbol{\Phi}_{WL} - \boldsymbol{P}_{NL} \tag{2.15}$$

2.3 Coordinate systems

Coordinate systems are fundamental for understanding the position of points in space. They provide a standardized way of describing a point's location in a given space. Some of the relevant coordinate systems for this thesis are described below.

2.3.1 Conventional Terrestrial Reference System (TRS)

The Conventional TRS, also called Earth-centred Earth-fixed (ECEF), is a spatial reference system, meaning that different realisations and versions exist. All versions, however, have the origin at the centre of an estimated ellipsoid (representing the Earth), with the Z-axis pointing from the centre to the conventional terrestrial pole, the X-axis pointing through the cross-section of the prime meridian and the equator, and the Y-axis orthogonal to the Z and X axes forming a right-handed system [4]. The ECEF frame is depicted in Figure 2.2.

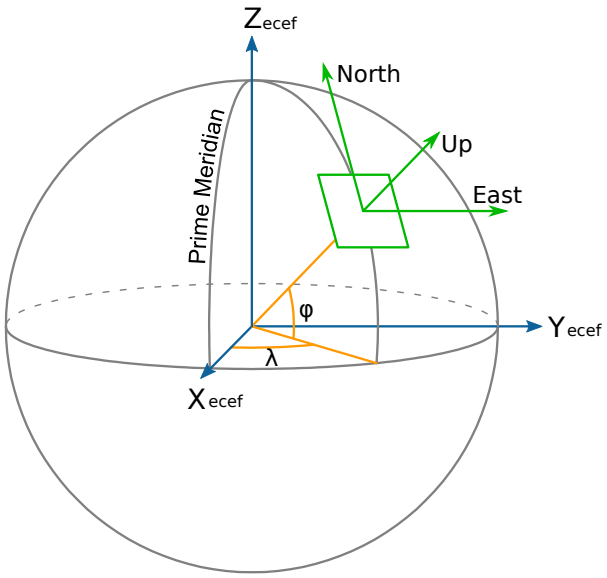

Figure 2.2: ECEF and ENU frames [1].

2.3.1.1 International Terrestrial Reference Frame (ITRF)

The ITRF is a realization of the ECEF produced by the International Earth Rotation and Reference Systems Service (IERS). It is a highly accurate and stable coordinate system in geodesy and Earth science for global reference [4].

2.3.1.2 East, North, Up (ENU)

The ENU coordinates are horizontal coordinates based on geographical location and are thus local. The 'East' and 'North' represent directions on the Earth's surface, while 'Up' points towards the sky, perpendicular to the Earth at the location. This coordinate system is widely used to describe horizontal errors in GNSS positioning [4]. The ENU frame is depicted together with the TRS frame in Figure 2.2.

2.3.1.3 Geodetic

Coordinates in an ECEF frame can be expressed as longitude, latitude and height above the reference ellipsoid. In Figure 2.2, the latitude and longitude components can be seen as φ and λ, respectively.

2.4 GNSS Error Sources

GNSS positioning suffers from several error sources, which will be covered in this section.

2.4.1 Emission and Reception Time

In order to accurately determine a receiver's position using GNSS algorithms, it is necessary to know the precise coordinates of the satellites at the time of signal emission. During the signal transmission time, i.e. the time it takes for the signal to travel from the satellite to the receiver, the satellites travel about 300 meters [4]. Without considering the transmission time, disturbances of up to 50 meters in the horizontal and vertical direction can occur [4]. To handle this error, the emission time has to be determined to calculate the satellite coordinates. The emission time can be calculated according to Equation (2.17) using the pseudorange measurement.

$$\Delta t_{tp} = \frac{P}{c} \tag{2.16}$$

$$t^s[emission] = t_r[reception] - \Delta t_{tp} \tag{2.17}$$

Where

- Δt_{tp} is the travel time of the signal calculated using the pseudorange
- $t^s[emission]$ is the time of signal emission from the satellite
- $t_r[reception]$ is the time of signal reception in the receiver.

2.4.2 Earth Rotation

As the signal travels from the satellite, the earth will rotate, meaning there will be a difference between the receiver position at the time of emission and reception if an ECEF frame is used. This will affect the estimated position, adding an offset of about 25 meters to the east. Equation (2.21) corrects the satellite position regarding this effect [4].

$$\mathbf{R}(\theta) = \begin{bmatrix} \cos(\theta) & \sin(\theta) & 0 \\ -\sin(\theta) & \cos(\theta) & 0 \\ 0 & 0 & 1 \end{bmatrix} \tag{2.18}$$

$$\Delta t_{tg} = \frac{\|\mathbf{r}^s - \mathbf{r}_r\|}{c} \tag{2.19}$$

$$\delta\vartheta = \omega_e \Delta t_{tg} \tag{2.20}$$

$$\tilde{\mathbf{r}}^s = \mathbf{R}(\delta\vartheta) \cdot \mathbf{r}^s \tag{2.21}$$

Where

- $\mathbf{R}$ is the rotation matrix of the earth around the z-axis
- ω_e is the rotation speed of the earth
- $\delta\vartheta$ is the rotation angle of the earth during the travel time of the signal
- Δt_{tg} is the travel time of the signal using the geometric distance to the satellite
- $\mathbf{r}^s$ is the position in the ECEF frame of the satellite
- $\tilde{\mathbf{r}}^s$ is the corrected position of the satellite adjusted by the earth's rotation.

2.4.3 Relativistic Effects

According to Einstein's theory of special relativity, two clocks travelling at different speeds will experience time dilation, meaning that the clocks will advance at different speeds. The faster an object moves relative to an observer, the slower it will appear to tick for the observer. Since the satellites travel at about 5km/s, this effect will be noticeable [4]. Another relativistic effect that affects GNSS positioning is from Einstein's theory of general relativity, which predicts the time dilation of two clocks placed at different distances from a gravitational mass. The closer a clock is to a gravitational mass relative to an observer, the slower the clock will appear to tick.

These effects must be accounted for since they can affect the position by tens of metres [4]. The special relativistic effect, which has the largest influence, can be cancelled with Equation (2.22), which corrects the GNSS observables in Equations (2.3) and (2.5).

$$\Delta_{rel} = -2\frac{\mathbf{r}^s \cdot \mathbf{v}^s}{c} \tag{2.22}$$

Where

- $\mathbf{v}^s$ is the velocity in the ECEF frame of the satellite.

Applying Equation (2.23) corrects the general relativistic effect. However, this only affects the positioning by a couple of centimetres.

$$\Delta\rho_{rel} = \frac{2 \cdot GM_E}{c^2} \ln\left(\frac{r^s + r_r + r_r^s}{r^s + r_r - r_r^s}\right) \tag{2.23}$$

Where

- GM_E is Earth's gravitational constant
- r^s is the geocentric distance to the satellite
- r_r is the geocentric distance to the receiver
- r_r^s is the distance from the receiver to the satellite.

2.4.4 Cycle Slip

Cycle slips are sudden changes in the estimated number of cycles related to the carrier phase measurement due to a temporary signal loss between the receiver and satellite [4]. This loss of lock can be caused by a weak connection or an obstacle, such as a tall building.

Cycle slips can be discovered by either finding a data gap, i.e. a loss of data from a satellite, or an unexpected behaviour in the signal. There are multiple ways of detecting cycle slips, depending on how many frequencies are accessed. For a dual-frequency system, the geometry-free combination of the carrier phase measurements, shown in Equation (2.24) can be used as input data.

$$\Phi_I^s(k) = \Phi_1^s(k) - \Phi_5^s(k) \tag{2.24}$$

Where

- Φ_I^s is the geometry-free carrier phase measurement
- k is the epoch.

Unexpected behaviour in the signal can be detected by fitting a second-degree polynomial to the previous data samples. A cycle slip can be declared if a specified threshold is exceeded by comparing the predicted value of the next epoch with the actual value from the input data. Further, a cycle slip is declared when there is a data gap.

2.4.5 Antenna Phase Centre (APC)

The APC represents the radiation source, which does not have to align with the physical centre of the antenna [4]. Instead, the APC depends on the frequency and angle of the signal, as depicted in Figure 2.3. The difference between the physical centre, or antenna reference point, and the APC is called the Antenna Phase Offset (APO) and is also shown in the figure. This phenomenon is present in both the satellite and receiver antennas.

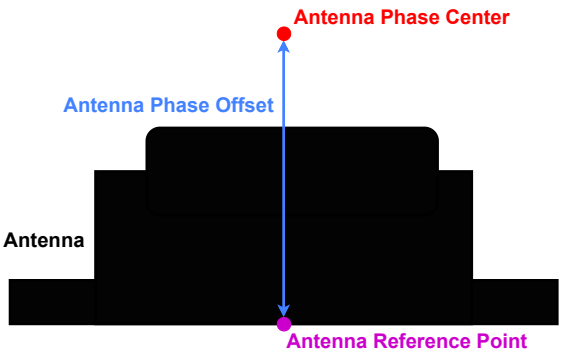

Figure 2.3: Simplified depiction of a receiver antenna with the corresponding antenna phase centre, antenna phase offset and antenna reference point.

Some corrections for the related error sources, such as clock and orbit errors, refer to the satellite mass centre, not the APC. The offset between the two points, Δ_{APC}, is in a satellite-fixed coordinate frame, which has to be recalculated to the ECEF reference frame. The recalculation is based on the unit vectors $(\hat{\boldsymbol{i}}, \hat{\boldsymbol{j}}, \hat{\boldsymbol{k}})$ that define the satellite-fixed coordinates. These unit vectors are defined in Equations (2.25) to (2.27).

$$\hat{\boldsymbol{k}} = -\frac{\mathbf{r}^{sMC}}{\|\mathbf{r}^{sMC}\|} \tag{2.25}$$

$$\hat{\boldsymbol{j}} = \hat{\boldsymbol{k}} \times \frac{\mathbf{r}_{sun} - \mathbf{r}^{sMC}}{\|\mathbf{r}_{sun} - \mathbf{r}^{sMC}\|} \tag{2.26}$$

$$\hat{\boldsymbol{i}} = \hat{\boldsymbol{j}} \times \hat{\boldsymbol{k}} \tag{2.27}$$

Where

- $\hat{\boldsymbol{k}}$ is the vector pointing to the centre of Earth from the mass centre
- $\hat{\boldsymbol{j}}$ is the cross-product between $\hat{\boldsymbol{k}}$ and the unit vector from the satellite to the sun
- $\hat{\boldsymbol{i}}$ is the cross-product between $\hat{\boldsymbol{j}}$ and $\hat{\boldsymbol{k}}$.

The satellite APC in ECEF coordinates is calculated with Equation (2.28).

$$\mathbf{r}^{sAPC} = \mathbf{r}^{sMC} + \mathbf{R} \cdot \Delta_{APC} \tag{2.28}$$

Where $\mathbf{R} = [\hat{\boldsymbol{i}}\ \hat{\boldsymbol{j}}\ \hat{\boldsymbol{k}}]$.

2.4.6 Atmospheric Effects

When a satellite broadcasts a GNSS signal to a receiver on Earth, the signal passes through the Earth's atmosphere. During this process, the signal is refracted and delayed, which causes a slight change in direction and impacts the signal's speed [15]. These changes result in errors when determining the receiver position and thus must be handled.

In Figure 2.4, the different layers of the atmosphere are depicted with their different heights, temperature and electron density. The primary source of error arises as the signal traverses through the ionosphere and the troposphere. However, the reasons for these errors differ and will be elaborated upon in the following subsections [15].

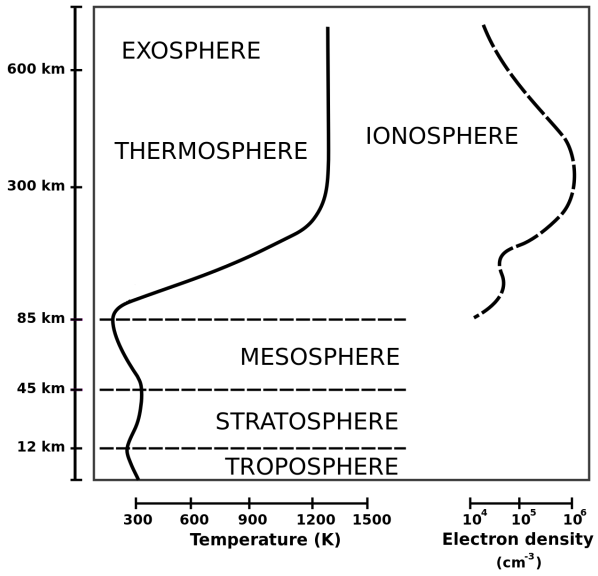

Figure 2.4: Atmospheric layers with their height, temperature and electron density [2].

2.4.6.1 Ionosphere

The main reason for the instabilities in the GNSS signal is the Earth's ionosphere [16]. The ionosphere is a layer in the Earth's atmosphere that gets ionized due to the sun's ultraviolet radiation. This ionization process releases free electrons, causing the atmosphere's density to fluctuate. This fluctuation is the primary cause of signal delay [16]. Figure 2.4 depicts the general electron density for different altitudes. The ionosphere's Total Electron Content (TEC) varies throughout the day and year, making it a challenging variable to estimate accurately and may cause errors [16].

The ionosphere is what is called a dispersive medium, meaning that RF signals of different frequencies will propagate through it at different speeds. This property makes it possible to estimate the ionosphere's electron content, which could be used when estimating a position [4].

2.4.6.2 Troposphere

The troposphere, the closest atmospheric region to Earth, as seen in Figure 2.4, affects the signal locally, meaning it is hard to use estimations from stations far away [4]. The tropospheric delay, $T(\epsilon)$, consists of two parts and can be written as:

$$T(\epsilon) = ZHD \cdot m_h(\epsilon) + ZWD \cdot m_w(\epsilon) \tag{2.29}$$

Where

- *ZHD* is the zenith value for the hydrostatic (dry) delay
- *ZWD* is the zenith value for the wet delay
- m_h is the mapping function for the dry delay
- m_w is the mapping function for the wet delay.

The mapping functions m_h and m_w depend on how the troposphere is modelled. Figure 2.5 depicts a simplification of the tropospheric delay where the purpose of a mapping function would be to estimate the propagation of the signal through the troposphere.

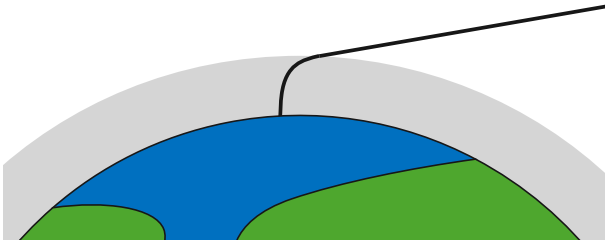

Figure 2.5: Simplification of tropospheric delay.

Contrary to the ionosphere, the troposphere is a non-dispersive medium for GNSS signals, meaning that the signal's frequency does not affect its travel speed [4]. Thus, the same corrections must be applied to the code and phase at different frequencies.

2.4.7 Multipath

A multipath error occurs when a signal sent from one satellite is received multiple times at a receiver, which causes interference [4]. This phenomenon can happen when the receiver is situated near large buildings or when the satellite is at a low elevation angle, causing the signal to bounce off the walls or the ground and reach the receiver from multiple directions, as illustrated in Figure 2.6.

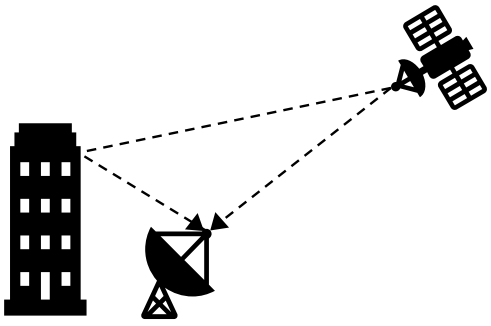

Figure 2.6: Illustration of multipath effect on GNSS signal.

For the code signal, multipath can theoretically cause errors as large as 450m, but the error is usually closer to two meters [4]. For the phase measurement, the error is commonly less than 1 cm.

2.4.8 Receiver Noise

Receiver noise arises from either the hardware or the software in the receiver. Generally, the error due to receiver noise is approximately 1% of the signal's wavelength [17].

2.4.9 Clock Error

To estimate a position using satellites, a very precise clock is necessary at the satellite. Therefore, satellites have atomic clocks with a precision of $\Delta f/f \simeq 10^{-13}$ [4]. Even though the satellite clocks are very accurate, they tend to drift slightly. Even a small drift can affect the estimated position greatly when it is calculated by the receiver [16]. These errors can be corrected either by differencing between two receivers or by using clock corrections from compute stations [4].

2.4.10 Orbit Error

Similar to the satellite clock, it is necessary to know the position of the satellite to estimate a receiver's position. The satellites transmit parameters such that it is possible to calculate their position, but in most cases, it is not good enough for precise positioning [4]. Therefore, just like the satellite clocks, corrections are needed to handle these errors.

2.4.11 Hardware-induced biases

GNSS hardware has certain deficiencies that cause biases due to minor delays in the signal transmission from a satellite or in signal reception by a GNSS receiver [18]. As a result of these delays, events that should co-occur may become asynchronous. These biases can vary between code signals (code bias) and carrier waves (known as phase bias). If these effects are not dealt with properly, they can impair the estimation of the receiver's position, extend the convergence time, and decrease the chance of integer ambiguity resolution.

2.4.11.1 Differential Code Bias (DCB)

DCBs are the time delays between two GNSS signals transmitted from a single satellite [18]. DCBs are expressed as in Equation (2.30) for the hardware delays between band i and j for satellite s. DCBs are often used as corrections retrieved from a computation centre when working with combinations of different frequencies.

$$DCB^s_{i,j} = b^s_i - b^s_j \tag{2.30}$$

2.4.12 Tidal Deformations

Due to the gravitational forces that the Earth is subject to, the crust deforms, thus moving the receiver's position. To mitigate this issue, modelling the displacement of

the Earth's crust is necessary. This displacement can be divided into solid tides, ocean loading, and pole tides. Solid tides cause the most significant offsets, hence, only these will be described.

2.4.12.1 Solid Tides

Solid tides refer to the movement of the Earth's crust due to external gravitational forces from the Sun and the Moon [4]. The displacement can be modelled as Equation (2.31) where $\Delta\mathbf{r}_{sol}$ needs to be applied to the receiver position [19].

$$\Delta\mathbf{r}_{sol} = \sum_{j=2}^{3} \frac{G\,M_j\,R_E^4}{G\,M_E\,R_j^3} \left(h_2\,\hat{\mathbf{r}} \left(\frac{3}{2}(\hat{\mathbf{R}}_j \cdot \hat{\mathbf{r}})^2 - \frac{1}{2} \right) + 3l_2\,(\hat{\mathbf{R}}_j \cdot \hat{\mathbf{r}}) \left(\hat{\mathbf{R}}_j - (\hat{\mathbf{R}}_j \cdot \hat{\mathbf{r}})\hat{\mathbf{r}} \right) \right) \tag{2.31}$$

Where

- $\Delta\mathbf{r}_{sol}$ is the displacement of the receiver
- GM_j is the gravitational constant of the Moon and the Sun, respectively
- GM_E is the gravitational constant of the Earth
- R_E is the radius of the Earth
- $\hat{\mathbf{R}}_j$ is the unit vector from the Earth to the Moon and Sun in ECEF, respectively
- R_j is the magnitude of the Moon and Sun position vectors
- r is the magnitude of $\mathbf{r}$
- h_2 is the nominal degree 2 Lovenumber
- l_2 is the nominal degree 2 Shilda number.

2.5 Extended Kalman Filter

The Extended Kalman Filter (EKF) is often used to estimate position in GNSS applications [20]. The EKF is based on the process equation in Equation (2.32) and the observation equation in Equation (2.33). The process equation describes how the states are expected to traverse from one time step to the next, with a known motion model, while the observation model describes the relationship between measurements and the state vector.

$$\boldsymbol{X}_k = \boldsymbol{f}_k(\boldsymbol{X}_{k-1}) + \boldsymbol{\nu}_k \tag{2.32}$$

$$\boldsymbol{Z}_k = \boldsymbol{h}_k(\boldsymbol{X}_k) + \boldsymbol{\omega}_k \tag{2.33}$$

Where

- $\boldsymbol{f}_k$ is the motion model
- $\boldsymbol{h}_k$ is the measurement model
- $\boldsymbol{\nu}_k \sim \mathcal{N}(0, \boldsymbol{Q}_k)$
- $\boldsymbol{\omega}_k \sim \mathcal{N}(0, \boldsymbol{R}_k)$.

The EKF uses the previous equations to form prediction and update steps. The prediction step uses a known motion model of the states and the previous state estimates to form the predicted (a priori) estimate. The prediction step also calculates a predicted covariance matrix $\boldsymbol{P}$ that describes the covariance of the predicted estimates. The prediction step is shown in Equations (2.34) and (2.35).

$$\hat{\boldsymbol{X}}_{k|k-1} = \boldsymbol{A}\hat{\boldsymbol{X}}_{k-1|k-1} \tag{2.34}$$

$$\boldsymbol{P}_{k|k-1} = \boldsymbol{A}\boldsymbol{P}_{k-1|k-1}\boldsymbol{A} + \boldsymbol{Q} \tag{2.35}$$

Where

- $\boldsymbol{A}_k = \frac{\partial \boldsymbol{f}_k}{\partial \boldsymbol{X}_{k-1|k-1}}$.

The update step uses the knowledge from Equation (2.33) to form a posterior update, meaning that it uses information from all time steps, including the current step, to form an updated estimation of the state vector and covariance matrix. The EKF uses a Kalman gain calculated based on the innovation covariance in Equation (2.37), observation model and predicted covariance. The Kalman gain dictates how certain measurements and predictions should be weighted based on covariance. The update step is shown in Equations (2.36)-(2.40).

$$\boldsymbol{v}_k = \boldsymbol{Z}_k - \boldsymbol{h}(\hat{\boldsymbol{X}}_{k|k-1}) \tag{2.36}$$

$$\boldsymbol{S}_k = \boldsymbol{H}_k\boldsymbol{P}_{k|k-1}\boldsymbol{H}^T + \boldsymbol{R}_k \tag{2.37}$$

$$\boldsymbol{K}_k = \boldsymbol{P}_{k|k-1}\boldsymbol{H}_k^T\boldsymbol{S}_k^{-1} \tag{2.38}$$

$$\hat{\boldsymbol{X}}_{k|k} = \hat{\boldsymbol{X}}_{k|k-1} + \boldsymbol{K}_k\boldsymbol{v}_k \tag{2.39}$$

$$\boldsymbol{P}_{k|k} = (\boldsymbol{I} - \boldsymbol{K}_k\boldsymbol{H}_k)\boldsymbol{P}_{k|k-1} \tag{2.40}$$

Where

- $\boldsymbol{H}_k = \frac{\partial \boldsymbol{h}_k}{\partial \boldsymbol{X}_{k|k-1}}$.

2.6 Satellite-Based Positioning

There are two main ways of constructing a GNSS solution, utilizing relative or absolute positioning.

2.6.1 Relative Positioning

Relative positioning involves the process of determining the location of a receiver (rover) by utilizing one or more stationary receivers, known as base stations, with pre-established positions.

2.6.1.1 Differential GNSS (DGNSS)

DGNSS is a relative positioning method using a stationary base station with a known location and a mobile rover, both of which act as receivers for the signals transmitted by GNSS satellites [21], as shown in Figure 2.7. The classical DGNSS method is based on calculating the pseudorange, see Section 2.2.1, for the receivers. Since the location of the base station is known, corrections can be calculated and transmitted to the rover. The pseudorange for the rover is calculated and the base station corrections are applied to improve the process of determining the position. This method can achieve a one-meter accuracy when the GPS constellation is used, provided the user is within a certain range, a few tens of kilometres from the reference station.

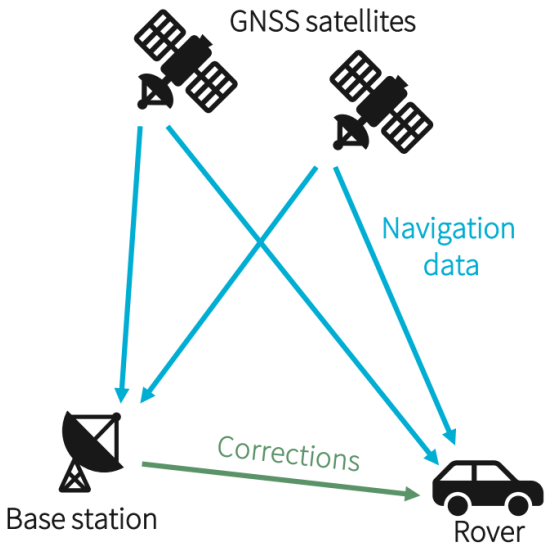

Figure 2.7: Simple depiction of relative positioning.

2.6.1.2 Real-Time Kinematic (RTK)

RTK orginated in the mid 1990s and is a type of DGNSS method that uses carrier-based ranging, meaning it can provide accurate positioning information but has to handle the ambiguities related to carrier phase measurements described in Section 2.2.2 [16], [4]. The RTK system can provide centimetre-level accuracy and includes a static base station and a mobile rover station, as shown in Figure 2.7.

Correction data, including atmospheric corrections, can be calculated and sent to the rover station along with the distance between the two, improving the estimation of the rover's position [16]. To access the corrections from a base station the rover must be in range and with minimal obstructions, as they reduce accuracy.

2.6.1.3 Network RTK

For RTK users who do not have their own base station, there is an alternative to buy a service called Network RTK. Network RTK uses multiple stationary base stations which send information regarding their positioning to a control centre [16]. The rover data is also sent to the central centre, where it is corrected based on the data provided by the network of base stations. This method is dependent on two-way communication between the centre and the rover and is depicted in Figure 2.8. The communication can be performed via Networked Transport of RTCM via Internet Protocol (NTRIP) if the receiver and the central centre have Internet access.

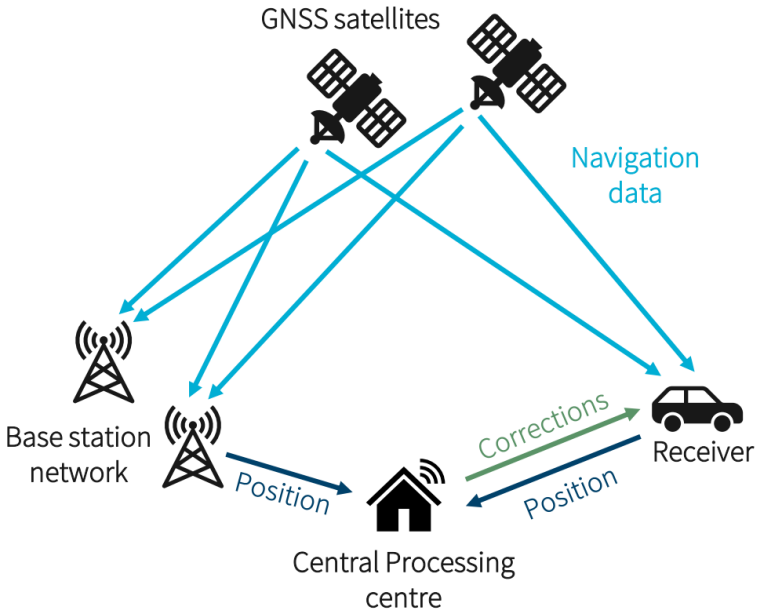

Figure 2.8: Simple depiction of Network RTK.

2.6.1.4 Wide Area RTK (WARTK)

WARTK is a concept to solve the range problem in RTK by providing the user with computations of an accurate ionosphere model to correct for the ionospheric errors, thus providing an expected range of hundreds of kilometres from the nearest base station. This is, however, only a concept, and no operational WARTK centres exist at this time [22].

2.6.2 Precise Point Positioning (PPP)

PPP is a technique used as an alternative to RTK positioning, where only one receiver is used [23]. It is not possible to differentiate between receivers, as only one is available. Unlike RTK, PPP does not require a base station to receive corrections. Instead, PPP uses a network of global reference stations that provide necessary satellite clocks and

orbital corrections (and biases), see Figure 2.9. The corrections from the global reference stations are then transmitted to the user either over satellite (L-band) or via the internet [16]. PPP uses both the pseudorange and carrier phase measurement to achieve high accuracy. PPP was introduced in 1997 by Zumberge, J et al. and has since continued to rise in popularity because of the lack of base station and freely available data [24],[25].

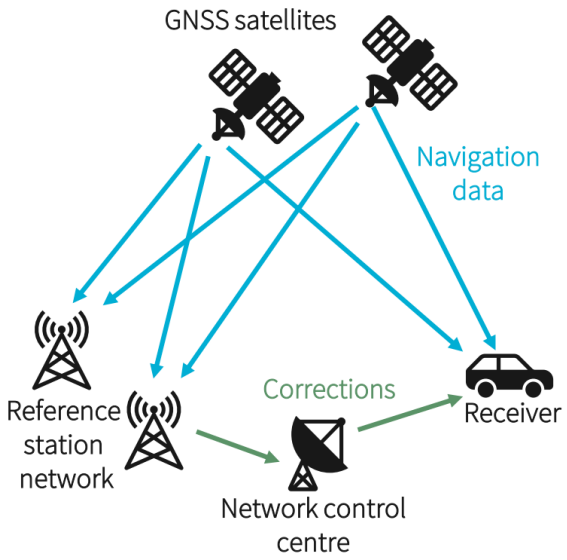

Figure 2.9: Precise positioning system.

There are different versions of PPP whose differences are discussed in the sections below.

2.6.2.1 Standard PPP

"Standard PPP" is a method that uses dual-frequency observables to form an IF combination, which eliminates almost all ionospheric disturbances [4]. This method does not fix the ambiguities to an integer number, instead, they will be floats. Float ambiguity is when the ambiguity is estimated together with the code biases and phase biases of the receiver and satellite, resulting in a float. This approach suffers from a long convergence time, as the ambiguities are not fixed [23]. The corrections used in this method can only be retrieved from the internet and are not available in real-time. Hence, this method is used for post-processing.

2.6.2.2 Ambiguity-fixed PPP

PPP with ambiguity resolution (or PPP-AR) is when an IF combination is used, and the ambiguities are fixed to integers, which can improve convergence time and accuracy [23]. Multiple methods for computing the integer ambiguity exist, one of which is described in the Method, see Section 3. The problem with both float and fixed ambiguity is that when an IF estimate is used, the noise increases substantially, making it harder to estimate a position. This is why these methods require a longer initialization time [26]. As this method uses the same corrections as the standard PPP, it is also only applicable as a post-processing method.

2.6.2.3 PPP-RTK

One disadvantage of standard PPP and PPP-AR is the long convergence time, however, recent studies have shown that a convergence time of a few seconds can deliver centimetre-level precision with the use of modern State Space Representation (SSR) corrections [5]. The modern SSR corrections do not only include the clock and orbital errors but also atmospheric effects, making it possible to not rely solely on the IF measurement, which has a substantial effect on noise levels [26]. Another advantage is that the SSR corrections are available in real-time and can be received via both satellite and the internet, making it the only solution possible to use in real-time systems.

2.7 Evaluation of GNSS Positioning

GNSS positioning can be evaluated in various ways. It is possible to calculate both an estimated accuracy, which shows what accuracy should be expected, and an actual accuracy, which shows how well the algorithm performs.

2.7.1 Vertical and horizontal accuracy

In GNSS, a receiver's positional accuracy is determined by its horizontal and vertical precision. Typically, the focus is on horizontal precision, which refers to the accuracy of the positioning in latitude and longitude. Conversely, vertical positioning indicates the accuracy of the height plane.

2.7.2 Dilution Of Precision (DOP)

DOP, or Dilution Of Precision, is a measure of the expected accuracy of a position calculated by a receiver [4]. The DOP value is derived solely from the estimated position of the receiver and the positions of the satellites. A high DOP value is observed when the tracked satellites are in close proximity to each other, making it challenging to estimate a position accurately. Conversely, a low DOP value is achieved when the satellites are widely dispersed, facilitating a more precise position estimation. Therefore, a lower DOP value (<5) is preferable as it yields a more accurate estimate [27].

There are several different DOP measurements, but the ones relevant to this thesis are the Horizontal DOP (HDOP) and the Vertical DOP (VDOP). To calculate the DOPs, the Line Of Sight (LOS) matrix has to be defined as in Equation (2.41), which includes the line of sight vector to every satellite n.

$$\mathbf{LOS} = \begin{bmatrix} \sin az_1 \cos el_1 & \cos az_1 \cos el_1 & \sin el_1 & 1 \\ \sin az_2 \cos el_2 & \cos az_2 \cos el_2 & \sin el_2 & 1 \\ \vdots & \vdots & \vdots & \vdots \\ \sin az_n \cos el_n & \cos az_n \cos el_n & \sin el_n & 1 \end{bmatrix} \tag{2.41}$$

Where

- az is the azimuth angle to the satellite
- el is the elevation angle to the satellite.

The DOP matrix is designed as the covariance matrix of the LOS matrix as in Equation (2.42).

$$\mathbf{Q} = \mathrm{Cov}(\mathbf{LOS}) = (\mathbf{LOS}^T\mathbf{LOS})^{-1} = \begin{bmatrix} q_{xx} & q_{xy} & q_{xz} & q_{xt} \\ q_{xy} & q_{yy} & q_{yz} & q_{yt} \\ q_{xz} & q_{yz} & q_{zz} & q_{zt} \\ q_{xt} & q_{yt} & q_{zt} & q_{tt} \end{bmatrix} \tag{2.42}$$

$$\mathbf{Q}_{ECEF} = \begin{bmatrix} q_{xx} & q_{xy} & q_{xz} \\ q_{xy} & q_{yy} & q_{yz} \\ q_{xz} & q_{yz} & q_{zz} \end{bmatrix} \tag{2.43}$$

To form the Q_{ENU} matrix, which is used for VDOP and HDOP, Q_{ECEF} from Equation (2.43), has to be transformed as shown in (2.44).

$$\mathbf{Q}_{ENU} = \mathbf{R}^T\mathbf{Q}_{ECEF}\mathbf{R} = \begin{bmatrix} q_{ee} & q_{en} & q_{eu} \\ q_{en} & q_{nn} & q_{nu} \\ q_{eu} & q_{nu} & q_{uu} \end{bmatrix} \tag{2.44}$$

Where

- R is the transformation matrix from ECEF to ENU at a given latitude and longitude.

The HDOP and VDOP can then be calculated according to Equations (2.45) and (2.46).

$$HDOP = \sqrt{q_{ee} + q_{nn}} \tag{2.45}$$

$$VDOP = \sqrt{q_{uu}} \tag{2.46}$$

3

Methods

This chapter provides an overview of the hardware used for collecting GNSS data. It also discusses the selection of positioning methods and the frequencies utilized. Additionally, it details the corrections applied and how they are implemented. The chapter includes information on the collection of data used for validating the implementation. It further describes the use of the Extended Kalman Filter for estimating receiver positions and the process for resolving ambiguities. The implementation is further outlined and visualized through flowcharts, followed by a comparison with the GNSS processing tool RTKLIB.

3.1 Hardware

One essential component of developing a complete GNSS solution is the receiver. For this project, the hardware was required to include an antenna for GNSS signals and a positioning module that could receive the raw GNSS data. The hardware was assessed based on the price, the frequencies it could receive, whether it could output raw GNSS data, the complexity of the setup process, and the performance. One receiver that met all the requirements and performed well in all the categories was the evaluation kit EVK-F9P from u-blox [28]. The evaluation kit included an ANN-MB antenna and a box containing a printed circuit board, both of which are shown in Figure 3.1. Mounted on the PCB was the u-blox ZED-F9P chip, a high-precision positioning module.

(a) EVK-F9P box **(b)** ANN-MB antenna

Figure 3.1: Receiver hardware.

The EVK-F9P was priced at around 3000 SEK, making it a low-cost module. The inclusion of an antenna in the kit made it cost-efficient and a good option to consider when taking the price into account. As the kit was complete, no further parts had to be purchased.

The ZED-F9P module is a dual-frequency receiver and can receive either L1/L2 or L1/L5 frequencies, depending on the model, EVK-F9P-01 or EVK-F9P-16 respectively. In both cases, it can output raw GNSS data, which was essential to this project. Being a dual-frequency receiver, it allows for combining the signals using the combinations described in Section 2.2.3. The model used in this thesis was the EVK-F9P-16, and the reasoning behind this decision is discussed further in Section 3.3.

The setup process was fairly fast and simple, partly due to the inclusion of an antenna, a straightforward connection with a USB-C cable and the u-blox GNSS evaluation software u-centre. As the kit was assembled upon delivery, the only setup necessary was connecting the antenna to the box, which was then connected to a computer where the evaluation software was downloaded and used to analyse the data. Some configuration was required to extract only the raw data from the module, which is explained in Appendix A.3.

The ZED-F9P module has been tested and proven to perform well in static PPP-RTK with L1/L2 frequencies [29], [30]. Good conditions resulted in high signal-to-noise (SNR) values and low multipath disturbances. With this module, it is possible to achieve high precision, with an accuracy of centimetres.

3.2 Positioning Method

The choice of positioning method for this project heavily depended on the application and the most recent advancements in the field, as this project aimed to drive further innovation in the GNSS area. RTK, which is introduced in the Theory Section 2.6.1.2, has been well explored. It relies on differencing between two receivers, eliminating the need for advanced corrections. The major drawback of RTK is the need for close proximity to a stationary base station with known coordinates. This means that if a rover requires a precise position in a large area (generally larger than a 10km radius), the performance of traditional RTK will greatly decrease due to atmospheric differences between the receivers. Sending corrections from a base station to a rover generally also demands clear LOS if RF is used, which means there can be no obstructions between the two. The corrections could, however, be sent via NTRIP, which would require Internet access for both the rover and the base.

Although PPP was first introduced in 1997, advancements are still being made. As discussed in the Theory Section, PPP was a post-processing method until recent years, when the corrections started to be readily available via NTRIP. These corrections are provided for free in real-time in the SSR format. PPP also has better scalability compared to network-RTK since no data has to be sent from the receiver to the reference stations, thus making it possible to have many users relying on the same corrections distributor. In the future, if self-driving cars become more common, this attribute will become more important since a lot of receivers demanding precise positions will be operational in tight areas, thus needing the same corrections.

PPP in real-time with SSR corrections (PPP-RTK) has been shown to produce results with a high accuracy and low convergence time, making it feasible to use in kinematic scenarios like in a car [5]. In the specified source, an accuracy of 0.1m in just 2 seconds is achieved 90% of the time in a kinematic scenario.

Since this thesis aimed to explore newer and promising areas in GNSS positioning, the focus lay on PPP. However, with the simplification of using precise products available for post-processing, which were used to simulate real-time corrections with a real-time algorithm. An ambiguity-fixing algorithm was researched and developed to fix ambiguities in a short time frame. Several sources describe that real-time ambiguity fixing is possible with proper corrections and can generate centimetre to decimetre accuracy [5], [23].

3.3 GNSS Frequencies

Since a two-frequency receiver was chosen, the choice of frequencies was between a combination of L1/L2 and L1/L5. L1/L2 would have been the most straightforward one since it is the most common combination, most corrections even refer to the ionosphere-free combination of L1/L2 [31]. However, the L5 signal, which is the most modern and should right now only be used at its own risk, is designed to be a safety-of-life signal with greater bandwidth to improve jam and multipath resistance [32].

As the L2 signal is older than L5, more satellites are capable of transmitting it. As of mid-2023, 17 out of 31 GPS satellites transmit L5 while 24 GPS satellites transmit L2 [33], all operational Galileo satellites transmit both E5b and E5a [34]. Since this report aimed to explore newer areas, the L5 signal was chosen in combination with L1.

3.4 GNSS Corrections

As described in the theory, the GNSS signals are affected by multiple sources of errors. For simplicity, the corrections of these errors were handled either offline, based on calculations of only the GNSS data or online, in relation to a filter estimation. Offline corrections were made for all steps of the observed data before the actual estimation of the position began, while online corrections were performed at each step. However, neither of the corrections relied on future data.

Corrections like the multipath and receiver noise were not handled explicitly in the implementation. The choice of location and placement of the antenna for the data collection mitigated the multipath. The risk of multipath occurring was significantly decreased by selecting a location without large disruptions, like buildings. The receiver noise is dependent on the type of receiver and antenna used. This noise was estimated together with the receiver clock bias.

3.4.1 Offline Corrections

The offline corrections were calculated for all time steps before the estimation of the position. Some of the error sources that were corrected offline were the emission time, earth rotation, relativistic effects and solid tides. The processes described in Sections

2.4.1-2.4.3 and 2.4.12.1 were followed to correct these errors, thus will not be covered in greater detail in this section.

3.4.1.1 Cycle Slip

Cycle slip detection was based on finding either a data gap or unexpected behaviour in the signal. The signal observed for the cycle slip detection was the difference between the frequencies of the carrier phase signals, i.e. $\mathbf{\Phi}_{slips} = \mathbf{\Phi}_1 - \mathbf{\Phi}_5$.

The data gap was identified when the last three data samples were unavailable. To find unexpected behaviour, a second-degree polynomial was fitted to the last 40 data samples, and the prediction of the next time step, based on this curve, was compared to the true value of the next time step. A cycle slip was declared if the difference between the two were larger than one meter.

3.4.1.2 Ionosphere

One of the significant atmospheric effects, the ionosphere, can be corrected using the ionosphere-free combination described in Paragraph 2.2.3.1. Equations 2.7 and 2.6 were used to calculate new code and phase measurements using frequencies L1 and L5.

3.4.1.3 Clock And Orbit Errors

The clock and orbit errors were corrected using precise orbit and clock corrections, which the Crustal Dynamics Data Information System (CDDIS) provides on a regular basis on the internet [35]. The orbit corrections are published at three intervals, ultra-rapid, rapid and final [36]. The three types of files are published 4 times per day, 17 hours after the end of the previous day and 13 days after the end of the solution week, respectively. These files differ in accuracy, with the most accurate being the final type. The clock corrections are only available in rapid and final form [37]. The final form of both the orbit and the clock corrections were utilised in this implementation.

The clock file contains the satellite clock error, dt^s, for all satellites recorded at specific intervals. In this case, the clock file had a 30-second interval. Since data collection occurred at 1Hz in this implementation, interpolation of the clock errors was necessary. A first-degree polynomial interpolation was employed to achieve centimetre-level accuracy in clock error estimations [4].

The orbit files provide the precise positions of all satellites in the ECEF coordinate system. Similar to the clock file, orbit files are generated at various intervals. Here, an orbit solution with a five-minute interval between data points was utilised. A 10-degree polynomial interpolation was applied to capture the dynamics of satellite movement accurately [4].

3.4.2 Online Corrections

Contrary to offline corrections, online corrections were calculated within the filter loop at each time step. Therefore, these corrections were dependent on the latest estimated position and could not be calculated beforehand.

3.4.2.1 Troposphere

There are multiple ways of determining the mapping functions mentioned in Section 2.4.6.2, m_h and m_w, depending on what input is available. One option is the *Mapping of Niell*, introduced in 1996 [38]. The hydrostatic mapping function, m_h, and the wet mapping function, m_w, are given by Equations (3.1) and (3.2).

$$m_h(el, H) = m(el, a_h, b_h, c_h) + \left(\frac{1}{sin(el)} - m(el, a_{ht}, b_{ht}, c_{ht}) \right) \cdot H \tag{3.1}$$

$$m_w(el) = m(el, a_w, b_w, c_w) \tag{3.2}$$

Where

- el is the elevation angle
- H is the height of the receiver.

a_w, b_w, c_w were determined through linear interpolation in Table A.2. a_{ht}, b_{ht}, c_{ht} can be found in Table A.1. a_h, b_h, c_h were calculated based on Equation (3.4) and linear interpolation of Table A.1.

$m(el, a, b, c)$ is the mapping normalized to unity at zenith [39], shown in Equation (3.3).

$$m(el, a, b, c) = \frac{1 + \frac{a}{1 + \frac{b}{1+c}}}{sin(el) + \frac{a}{sin(el) + \frac{b}{sin(el)+c}}} \tag{3.3}$$

The average and amplitude values correspond to ξ_{avg} and ξ_{amp} respectively in Equation (3.4) and were used to determine a_h, b_h, c_h through.

$$\xi(\phi, t) = \xi_{avg}(\phi) - \xi_{amp}(\phi) \cdot cos\left(2\pi \frac{t - T_0}{365.25}\right) \tag{3.4}$$

Where

- ϕ is the latitude of the receiver
- t is the day of year (DOY)
- T_0 is constant with a value of 28 for the northern hemisphere [40]
- ξ_{avg} and ξ_{amp} are given by linear interpolation from Table A.1.

The hydrostatic and wet delay, ZHD and ZWD, were determined using Equations (3.5) and (3.6) [40].

$$ZHD = 2.3 \cdot e^{-0.116 \cdot 10^{-3} \cdot H} \tag{3.5}$$

$$ZWD = ZWD_0 + \Delta ZWD \tag{3.6}$$

Where

- $ZWD_0 = 0.1$
- ΔZWD is estimated as a random walk process.

3.5 Data Collection

GNSS data was needed to test and validate the implementation of the corrections as well as the entire system. The tests included analysing how the different corrections affect the accuracy, how fast the solution converges, and the overall accuracy the system could achieve. As implied by the project's limitations, the data was only collected in a stationary scenario. The data was acquired with the receiver described in Section 3.1, the EVK-F9P evaluation kit.

The data collection took place on March 4, 2024, in Mölndal, Sweden, on the roof of a building. The collection began at 17.29 UTC+1 and ended at 23.59 UTC+1. The site was expected to be a low-multipath environment due to the height of the receiver placement. The receiver was set to have a 1Hz reception frequency and to output raw data, the u-blox SFBRX and RAWX messages [41]. However, only the RAWX messages were used in this project as they contained the pseudoranges and carrier phase measurements.

The ionospheric effect can be monitored through a service provided through the national network of stationary reference stations SWEPOS [42], which allows for real-time and historical ionosphere monitoring. The ionospheric effect during the day of the data collection session is visualized in Figure 3.2. These graphs depict the ionosphere changes in the Götaland region, a region in the south of Sweden, where Mölndal is located.

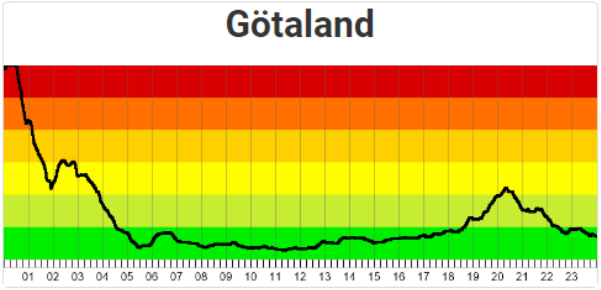

Figure 3.2: Illustration of the ionospheric effect during 04-03-2024 where the bottom row indicates the hour of the day in UTC+1 [42].

The colours in the figure represent how much the ionosphere affects the uncertainty of the measurements. The top two red regions indicate high uncertainty, making the measurements difficult to trust. In the two middle rows, the uncertainty gradually decreases. The bottom two rows, the green region, imply a low uncertainty.

During the data collection period, 17.29 to 23.59 UTC+1, the ionospheric effects were relatively low, with a slight elevation around 19 to 21 UTC+1, as seen in Figure 3.2.

3.6 Extended Kalman Filter

The developed solution equipped an EKF to estimate the position, a popular filter choice according to [20]. It was not possible to use a regular Kalman filter in this application since the measurement equations in (2.3) and (2.5) are non-linear with respect to the position of the receiver, which needs to be estimated as a state. The EKF, described in Section 2.5, forms the Kalman matrices by linearising the process- and measurement-equation around an operating point at each time step. In this case, only the measurement equation had to be linearised since the process function was linear, as described further down in this section. The state vector in the developed EKF, shown in Equation (3.8), contained the positional states δx, δy and δz that described the change in position between time steps. The actual estimated position in ECEF at time step k was therefore retrieved by Equation (3.7).

$$\tilde{\boldsymbol{r}}_k = \begin{bmatrix} \delta x_k & \delta y_k & \delta z_k \end{bmatrix}^T + \tilde{\boldsymbol{r}}_{k-1} \tag{3.7}$$

The state vector also included the states cdt_r, which is the receiver clock bias combined with the light speed factor to produce an estimate in meters. An inter system bias, b_{ISB}, between GPS and Galileo, was also included since there could be biases between the different constellations. The second to last state to be estimated was the change in ZWD, ΔZWD. The last states, denoted $\tilde{\boldsymbol{N}}_{IF}$, are the float ambiguities from the ionosphere-free combination of carrier phase measurements.

$$\boldsymbol{X} = \begin{bmatrix} \delta x & \delta y & \delta z & cdt_r & b_{ISB}^{gal} & \Delta ZWD & \tilde{\boldsymbol{N}}_{IF} \end{bmatrix}^T \tag{3.8}$$

The measurement vector was designed as in Equation (3.9), where some of the corrections were applied. Note that the variables with a superscript of gal or gps denote all of the satellites from either Galileo or GPS.

$$\boldsymbol{Z} = \begin{bmatrix} \boldsymbol{P}_{IF}^{gal} \\ \boldsymbol{P}_{IF}^{gps} \\ \boldsymbol{\Phi}_{IF}^{gal} \\ \boldsymbol{\Phi}_{IF}^{gps} \end{bmatrix} = \begin{bmatrix} \boldsymbol{P}_{IF,raw}^{gal} + \boldsymbol{dt}^{gal} - \boldsymbol{\Delta}_{rel}^{gal} - \boldsymbol{T}_p^{gal} \\ \boldsymbol{P}_{IF,raw}^{gps} + \boldsymbol{dt}^{gps} - \boldsymbol{\Delta}_{rel}^{gps} - \boldsymbol{T}_p^{gps} \\ \boldsymbol{\Phi}_{IF,raw}^{gal} + \boldsymbol{dt}^{gal} - \boldsymbol{\Delta}_{rel}^{gal} - \boldsymbol{T}_p^{gal} \\ \boldsymbol{\Phi}_{IF,raw}^{gps} + \boldsymbol{dt}^{gps} - \boldsymbol{\Delta}_{rel}^{gps} - \boldsymbol{T}_p^{gps} \end{bmatrix} \tag{3.9}$$

Where

- $\boldsymbol{T}_p^{sys} = ZHD \cdot \boldsymbol{m}_h^{sys} + ZWD_0 \cdot \boldsymbol{m}_w^{sys}$ is the partial tropospheric correction.

The prediction step was executed using the process matrix, denoted as A in Equation (3.10). This matrix corresponded to a kinematic model for the positional states, implying that these states are independent of their preceding values. The process noise matrix, Q in Equation (3.11), describes the uncertainties of the process model. For the positional states, an uncertainty of 1m was chosen even if the position of the receiver was known to be stationary. Since the sampling frequency was 1Hz, this resulted in a variance of 1m/s. The receiver clock error, inter system bias and tropospheric uncertainty were chosen based on literature and results. The ambiguities were designed to equal their previous value with no uncertainty since they are constant as long as no cycle slip occurs.

$$\boldsymbol{A} = diag\left(\mathbf{0}_5, \quad \mathbf{1}_{n+1}\right) \tag{3.10}$$

$$\boldsymbol{Q} = diag\left(\mathbf{1}_3, \quad 1e^6, \quad 1e^{-2}, \quad 0.2, \quad \mathbf{0}_n\right) \tag{3.11}$$

The initial uncertainties needed for the Kalman filter were as written in (3.12). The initial uncertainty was redundant for the states with a zero in the process matrix A due to the formula in Equation (2.35). The initial uncertainty for the ambiguities was set to a large value such that they quickly adapted to the measurement.

$$\boldsymbol{P_0} = diag\left(\mathbf{0}_6, \quad \mathbf{1}_n \cdot 10^{10}\right) \tag{3.12}$$

To retrieve the observation matrix, $\boldsymbol{H}$, the measurement equations (Equations (2.5) and (2.3)) had to be differentiated with respect to the states as in Equation (3.13).

$$\boldsymbol{H} = \begin{bmatrix} \frac{\partial P_{IF}^{gal,0}}{\partial x_0} & \cdots & \frac{\partial P_{IF}^{gal,0}}{\partial x_n} \\ \vdots & \ddots & \vdots \\ \frac{\partial P_{IF}^{gal,i}}{\partial x_0} & \cdots & \frac{\partial P_{IF}^{gal,i}}{\partial x_n} \\ \frac{\partial P_{IF}^{gps,0}}{\partial x_0} & \cdots & \frac{\partial P_{IF}^{gps,0}}{\partial x_n} \\ \vdots & \ddots & \vdots \\ \frac{\partial P_{IF}^{gps,j}}{\partial x_0} & \cdots & \frac{\partial P_{IF}^{gps,j}}{\partial x_n} \\ \frac{\partial \Phi_{IF}^{gal,0}}{\partial x_0} & \cdots & \frac{\partial \Phi_{IF}^{gal,0}}{\partial x_n} \\ \vdots & \ddots & \vdots \\ \frac{\partial \Phi_{IF}^{gal,i}}{\partial x_0} & \cdots & \frac{\partial \Phi_{IF}^{gal,i}}{\partial x_n} \\ \frac{\partial \Phi_{IF}^{gps,0}}{\partial x_0} & \cdots & \frac{\partial \Phi_{IF}^{gps,0}}{\partial x_n} \\ \vdots & \ddots & \vdots \\ \frac{\partial \Phi_{IF}^{gps,j}}{\partial x_0} & \cdots & \frac{\partial \Phi_{IF}^{gps,j}}{\partial x_n} \end{bmatrix} = \begin{bmatrix} \frac{x_r - x^{gal,0}}{\rho^0} & \frac{y_r - y^{gal,0}}{\rho^0} & \frac{z_r - z^{gal,0}}{\rho^0} & 1 & 1 & mw^{gal,0} & 0 & \dots & 0 \\ & & \vdots & & & & & \ddots & \\ \frac{x_r - x^{gal,i}}{\rho^i} & \frac{y_r - y^{gal,i}}{\rho^i} & \frac{z_r - z^{gal,i}}{\rho^i} & 1 & 1 & mw^{gal,i} & 0 & \dots & 0 \\ \frac{x_r - x^{gps,0}}{\rho^0} & \frac{y_r - y^{gps,0}}{\rho^0} & \frac{z_r - z^{gps,0}}{\rho^0} & 1 & 0 & mw^{gps,0} & 0 & \dots & 0 \\ & & \vdots & & & & & \ddots & \\ \frac{x_r - x^{gps,j}}{\rho^j} & \frac{y_r - y^{gps,j}}{\rho^j} & \frac{z_r - z^{gps,j}}{\rho^j} & 1 & 0 & mw^{gps,j} & 0 & \dots & 0 \\ \frac{x_r - x^{gal,0}}{\rho^0} & \frac{y_r - y^{gal,0}}{\rho^0} & \frac{z_r - z^{gal,0}}{\rho^0} & 1 & 1 & mw^{gal,0} & 1 & \dots & 0 \\ & & \vdots & & & & & \ddots & \\ \frac{x_r - x^{gal,i}}{\rho^i} & \frac{y_r - y^{gal,i}}{\rho^i} & \frac{z_r - z^{gal,i}}{\rho^i} & 1 & 1 & mw^{gal,i} & 0 & \dots & 1 \\ \frac{x_r - x^{gps,0}}{\rho^0} & \frac{y_r - y^{gps,0}}{\rho^0} & \frac{z_r - z^{gps,0}}{\rho^0} & 1 & 0 & mw^{gps,0} & 1 & \dots & 0 \\ & & \vdots & & & & & \ddots & \\ \frac{x_r - x^{gps,j}}{\rho^j} & \frac{y_r - y^{gps,j}}{\rho^j} & \frac{z_r - z^{gps,j}}{\rho^j} & 1 & 0 & mw^{gps,j} & 0 & \dots & 1 \end{bmatrix} \tag{3.13}$$

The measurement noise shown in Equation (3.14) depended on the elevation angle of the satellite, el, where a greater elevation angle resulted in a lower noise level on the measurement. The first entry in $\boldsymbol{R}$ accounted for the pseudorange measurements with a higher noise and the latter for all the carrier phase measurements with lesser noise.

$$\boldsymbol{R} = diag\left(0.5^2 + \frac{0.5^2}{\sin(\boldsymbol{el})^2}, \quad 0.001^2 + \frac{0.001^2}{\sin(\boldsymbol{el})^2}\right) \tag{3.14}$$

Where

- $\boldsymbol{el}$ is the vector containing the elevation angle for all satellites.

In the EKF loop, it was necessary to handle cycle slips, as detailed in 2.4.4. This is due to the fact that measurements affected by cycle slips can negatively impact the accuracy of the position estimate. This negative effect occurs because the ambiguity linked to the cycle-slipped measurement will be incorrect, essentially forcing the other states to adjust in response. When a cycle slip was detected, increasing the uncertainty of the ambiguity associated with the cycle-slipped measurement was required. This allowed the ambiguity to be re-estimated and assigned a new, more accurate value. In practical terms, this was achieved by augmenting the uncertainty in the $\boldsymbol{P}$ matrix within the EKF loop specifically for the ambiguity state. This adjustment helped mitigate the effects of cycle slips and maintained the precision of the position estimate.

A robust weighing function was also developed based on the innovation such that outliers were rejected, and estimations with a low innovation would be weighted more. The function is described in Equation (3.15).

$$w(r_k) = \begin{cases} 1 & |r_k| \leq c_o \\ \frac{|r_k|}{c_o}\left(\frac{c_1 - c_o}{c_1 - |r_k|}\right)^2 & c_o < |r_k| \leq c_1 \\ \infty & |r_k| > c_1 \end{cases} \tag{3.15}$$

Where

- r_k is the standardised residuals of the innovation $r_k = \frac{\boldsymbol{v}_k - E[\boldsymbol{v}_k]}{Var[\boldsymbol{v}_k]}$
- c_0 is a constant with a value of 1
- c_1 is a constant with value 100 for pseudorange measurements and 4 for carrier phase measurements.

This resulted in a weight equal to one for the measurements close to the mean of the innovation, a medium weight was applied to the measurements that were in the vicinity of the mean of the innovation most likely due to noise. An infinite weight was applied to the measurements that were far away from the mean of the innovation, as they most likely were outliers.

After the prediction and update steps were performed, the ambiguities had to be fixed to get a precise result. The ambiguity resolution is described in the next section.

3.7 Ambiguity Resolution

Ambiguity resolution in GNSS is a crucial process in PPP to accurately and quickly determine the distance to a satellite using carrier-phase measurement. The process consists of separating the receiver and satellite's float biases with an integer ambiguity term.

The process of fixing the ambiguities was based on Single Differenced (SD) measurements using a reference satellite. The reference satellite was chosen based on its elevation angle. In the first time step, the satellite with the largest elevation angle, i.e., closest to the zenith, was chosen. The same satellite was used until it reached a 20-degree elevation angle or a cycle slip was detected for the specific satellite. The GNSS constellations were handled separately; hence, one Galileo and one GPS reference satellite were chosen.

One method of fixing the ambiguities handles the wide-lane and narrow-lane ambiguities consecutively [43]. The first step is to fix the wide-lane ambiguities. The float narrow-lane ambiguities are calculated based on the fixed wide-lane ambiguities and fixed using the Least-Squares Ambiguity Decorrelation (LAMBDA) method [44]. A modified LAMBDA (MLAMBDA) method can also be used. MLAMBDA is a faster and less computationally complex method [45]. Finally, the fixed WL and NL ambiguities are combined to determine the fixed IF ambiguities. Handling the WL and NL ambiguities consecutively eliminates the receiver phase bias, and the satellite phase biases are corrected. This described method was used and explained below.

3.7.1 Wide-Lane Ambiguity Fixing

The Melbourne-Wübbena (MW) combination, see Equation 2.15, was used to fix the WL ambiguities. The SD MW measurements, $\tilde{\boldsymbol{MW}}_{SD}$, were calculated as suggested by Equations (3.16)-(3.18). The SD operation removed the receiver hardware bias, leaving only the satellite hardware bias.

$$\boldsymbol{MW}_{SD}^{gal} = \boldsymbol{MW}^{gal} - MW_{ref}^{gal} \tag{3.16}$$

$$\boldsymbol{MW}_{SD}^{gps} = \boldsymbol{MW}_{gps} - MW_{ref}^{gps} \tag{3.17}$$

$$\tilde{\boldsymbol{MW}}_{SD} = \begin{bmatrix} \boldsymbol{MW}_{SD}^{gal} & \boldsymbol{MW}_{SD}^{gps} \end{bmatrix}^T \tag{3.18}$$

The fixed WL ambiguities were calculated by fixing $\tilde{\boldsymbol{MW}}_{SD}$. Due to the long wavelength, the $\tilde{\boldsymbol{MW}}_{SD}$ was fixed by rounding the average of the last 5 time steps to an integer as shown in Equation (3.19).

$$\boldsymbol{MW}_{fixed} = \boldsymbol{WL}_{fixed} = round(\langle \tilde{\boldsymbol{MW}}_{SD} + b_{WL,SD}^{s} \rangle_5) \tag{3.19}$$

Where

- $b_{WL,SD}^{s}$ is the satellite hardware bias for WL combination [46].

3.7.2 Narrow-Lane Ambiguity Fixing

The next step was fixing the NL ambiguities by single differencing using the same reference satellites that were used when calculating the $\boldsymbol{M\tilde{W}}_{SD}$. The process shown in Equations (3.16)-(3.18) was repeated for the IF measurements, resulting in the IF SD float ambiguities $\tilde{\boldsymbol{N}}_{IF,SD}$. The NL float ambiguities were then calculated according to Equation (3.20), which combined the IF and WL float ambiguities [46].

$$\tilde{\boldsymbol{NL}}_{SD} = \tilde{\boldsymbol{N}}_{IF,SD}\frac{L1+L5}{\lambda_1 \cdot L1} - \boldsymbol{WL}_{fixed}\frac{L5}{L1-L5} + b^s_{NL,SD} \tag{3.20}$$

Where

- $b^s_{NL,SD}$ is the satellite hardware bias for NL combination.

The covariance of the IF SD float ambiguities, $\boldsymbol{P}_{IF,SD}$, was calculated according to Equation (3.21).

$$\boldsymbol{P}_{IF,SD} = \boldsymbol{D} \cdot \boldsymbol{P}_{IF} \cdot \boldsymbol{D}^T \tag{3.21}$$

Where $\boldsymbol{P}_{IF}$ is the covariance of the float IF ambiguities calculated by an EKF, and $\boldsymbol{D}$ is the SD design matrix. The size and layout of matrix $\boldsymbol{D}$ were dependent on the actual time steps number of satellites and the index of the reference satellites. $\boldsymbol{D}$ is a modified identity matrix where the columns of the reference satellites are -1 for the rows corresponding to the satellite in its constellation. Additionally, the rows with the indices of the reference satellites were removed. An example of how $\boldsymbol{D}$ can look is shown in Equation (3.22) where the reference satellite for Galileo has an index of 2 and for GPS has an index of 3, where the number of Galileo satellites is 3 and GPS satellites is 4.

$$\boldsymbol{D} = \begin{bmatrix} 1 & -1 & 0 & 0 & 0 & 0 & 0 \\ 0 & -1 & 1 & 0 & 0 & 0 & 0 \\ 0 & 0 & 0 & 1 & 0 & -1 & 0 \\ 0 & 0 & 0 & 0 & 1 & -1 & 0 \\ 0 & 0 & 0 & 0 & 0 & -1 & 1 \end{bmatrix} \tag{3.22}$$

The covariance of the NL float ambiguities, $\boldsymbol{P}_{NL,SD}$, was then determined using the covariance propagation law as in Equation (3.23).

$$\boldsymbol{P}_{NL,SD} = \frac{1}{(\lambda_{NL})^2}\boldsymbol{P}_{IF,SD} \tag{3.23}$$

Where

- $\lambda_{NL} = \frac{c}{L1+L5}$ is the wavelength of the narrow-lane combination.

Since the $\tilde{\boldsymbol{NL}}_{SD}$ ambiguities still were not fixed, the MLAMBDA method had to be used, which decorrelated and fixed the float ambiguities based on the ambiguities, $\tilde{\boldsymbol{NL}}_{SD}$, and their covariance, $\boldsymbol{P}_{NL,SD}$.

3.7.3 IF Ambiguity Fixing

Based on the result of the MLAMBDA function, $\boldsymbol{NL}_{fixed}$, and the fixed WL ambiguities, $\boldsymbol{WL}_{fixed}$, the final fixed ambiguities, $\boldsymbol{N}_{IF,fixed}$, were calculated according to Equation (3.24).

$$\boldsymbol{N}_{IF,fixed} = \lambda_{NL} \cdot \boldsymbol{NL}_{fixed} - \frac{\lambda_5}{\gamma_5 - 1} \boldsymbol{WL}_{fixed} \tag{3.24}$$

Where $\gamma_5 = f_1^2 / f_5^2$. After the ionosphere-free ambiguities were fixed, in the next time-step, the fixed ambiguities were used instead of the float ones until a cycle slip occurred and the fixing process needed to restart.

3.8 Implementation Overview

An overview of the implemented solution can be seen in Figure 3.3. The implementation included three parsers: one for the raw GNSS data, one for the precise clock and orbit products and one for the APO corrections. The parsed data from the input sources computed the offline corrections listed to the right in Figure 3.3. Based on these offline corrections, it was possible to calculate the DOP accuracies, including horizontal and vertical DOP, HDOP and VDOP. After the offline corrections, the estimation process was done using an EKF, which estimated the state vector in Equation (3.8) for each time step.

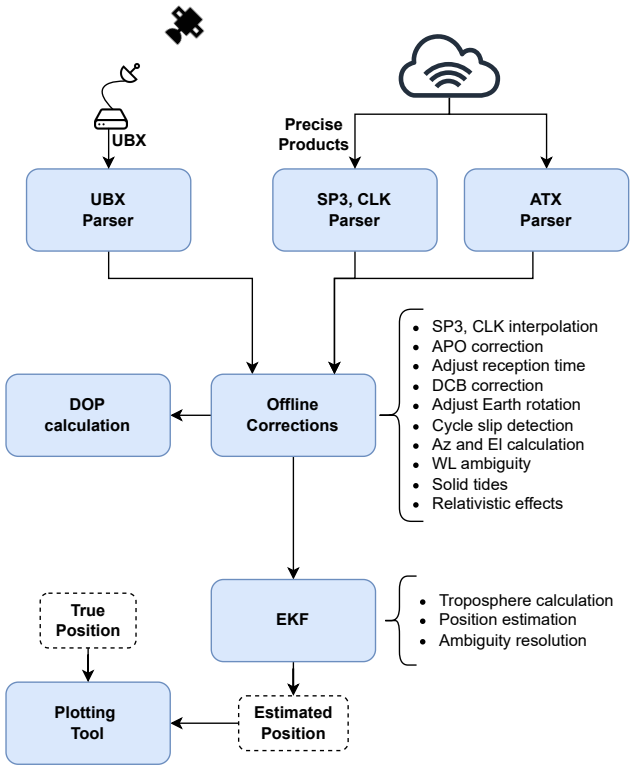

Figure 3.3: Overview of software structure.

The Extended Kalman Filter (EKF) is depicted in greater detail in Figure 3.4, beginning with the prediction and update phases, then proceeding to cycle slip management and ambiguity resolution. Upon detection of a cycle slip, the uncertainty of the associated ambiguity estimate was increased to mitigate its impact on other state estimates, as outlined in Section 3.6. Without a cycle slip, the process assessed whether the ambiguities have been fixed since a previous step, if they were fixed, continue with the same ambiguities. If the ambiguities were not fixed, try to fix them with ambiguity resolution and run the loop again.

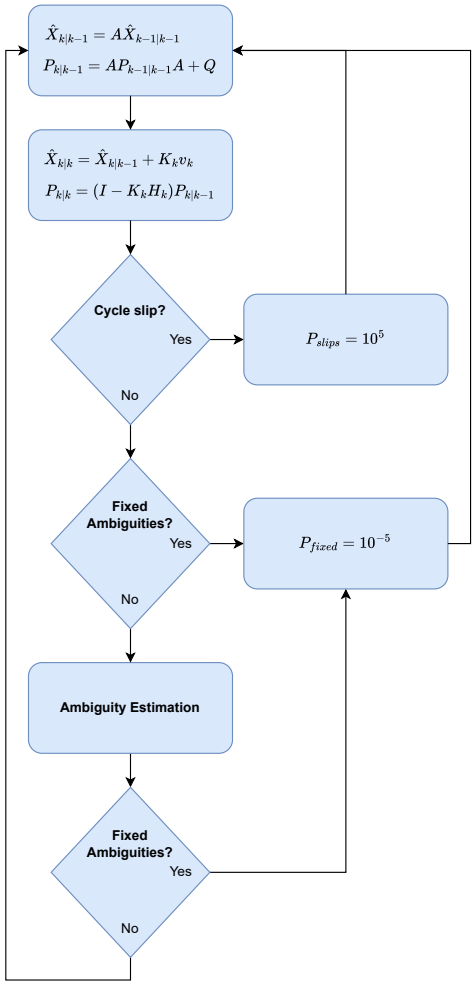

Figure 3.4: Overview of EKF.

3.9 Comparison

The implemented solution was compared to existing packages that process GNSS data. RTKLIB is a GNSS processing tool that can estimate position using several different modes, combinations and corrections [47]. The tool was configured to have the same information as the proposed solution, including precise orbit and clock files. The options for the tool are shown in Figure 3.5.

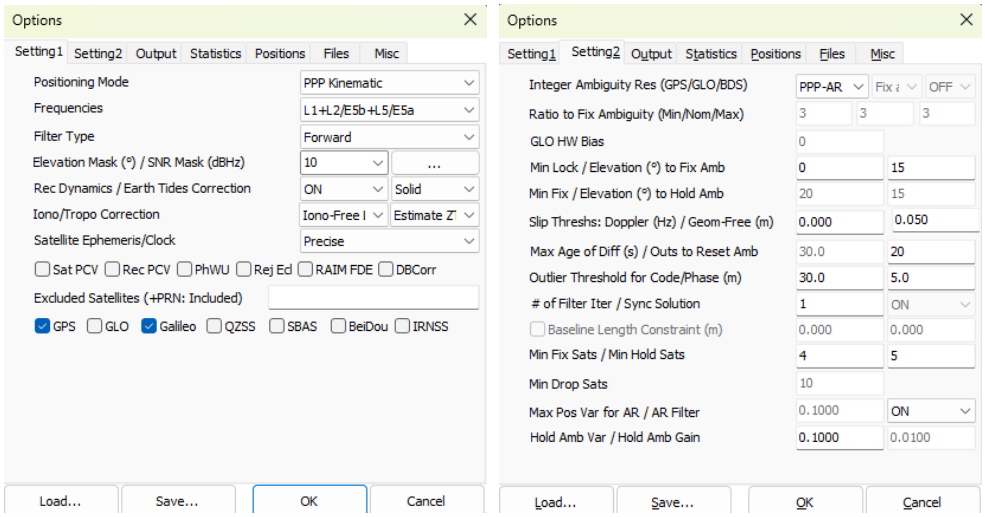

Figure 3.5: RTKLIB options that was used.

4

Results

This Chapter presents the outcomes of the applied corrections, the horizontal and vertical DOP values, and the estimated position's accuracy in horizontal and vertical form. The results from RTKLIB are also depicted. The Figures in this section are based on the data described in Section 3.5.

4.1 Corrections

The resulting effects of the implemented corrections are visualised in Figures 4.1-4.8. The amount of epochs included in each plot varies depending on how long the satellite is visible to the receiver. For the case where all satellite corrections are included in a single figure, the entire 19,000 time steps of data collection are visible.

The relativistic clock effect in meters is shown in Figure 4.1. The relativistic effects on each satellite that are included in the data are visible in the figure. The relativistic correction, Δ_{rel}, is applied to the pseudorange and carrier phase measurements, as shown in Equations (2.3) and (2.5). The effect of the relativistic clock varies in range between satellites. The smallest values are around 0m, while the largest effect for this data is around ±60m. Most values are within the ±7.5m range, depicted in Figure 4.2. The Figure presents a close-up of the same values as in Figure 4.1 and indicates that the correction behaves like a sinusoidal curve for each satellite.

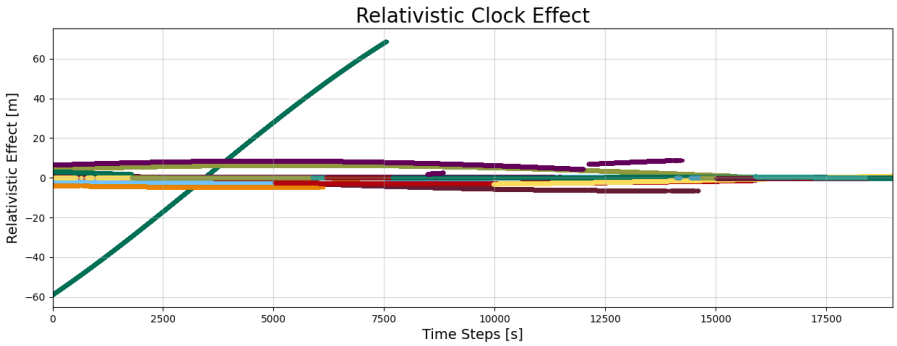

Figure 4.1: Relativistic clock effect in meters for all Galileo and GPS satellites in each time step.

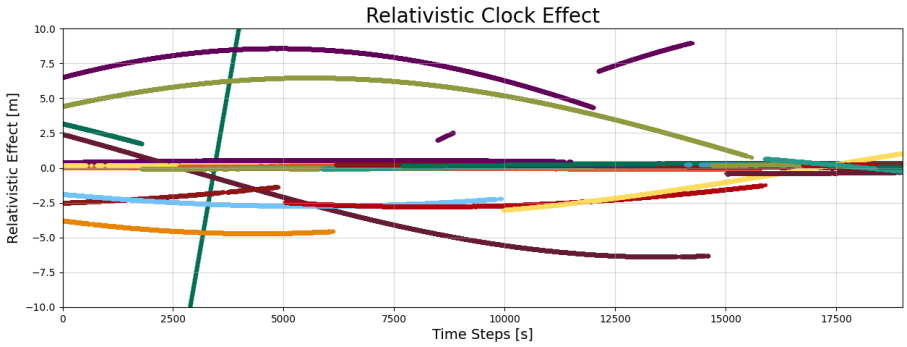

Figure 4.2: Close-up of relativistic clock effect in meters for all satellites in each time step.

Figure 4.3 depicts the effect of the solid tides. The Figure contains the correction in the X-, Y- and Z-directions (which correspond to the east, north and height directions) applied to the receiver position. The effect is relatively small and ranges between 0.2m and 0.7m.

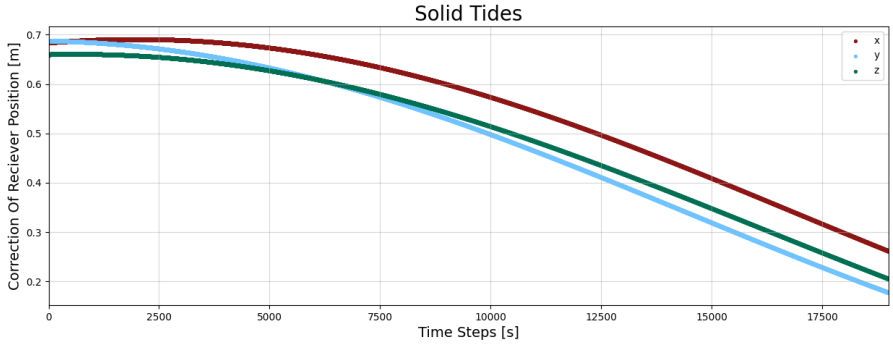

Figure 4.3: Solid Tides effect in meters for each time step.

The earth rotation correction for the position of one satellite is shown in Figure 4.4. Since the correction is consistent at around ±200m for all Galileo and GPS satellites, the behaviour of a single satellite is representative. The effect in the Z-direction is 0 for each satellite, as the earth's rotation only affects the position of the satellite relative to the receiver in the X- and Y-directions due to its rotation about the Z-axis.

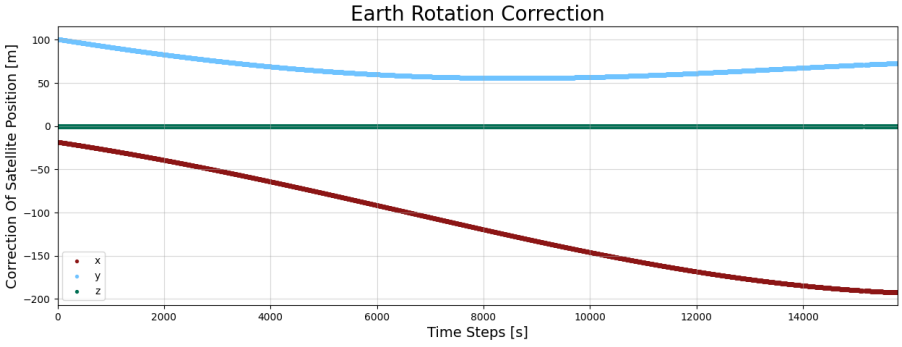

Figure 4.4: Earth Rotation effect in meters for 15,000 time steps for one satellite.

The satellite clock bias, dt^s, has an immense effect on the accuracy of the system, as visualised in Figure 4.5. The correction of the pseudorange and carrier phase measurements for all satellites in every time step is included. Most corrections are within the ±200,000m range and do not vary during the period of the collected data.

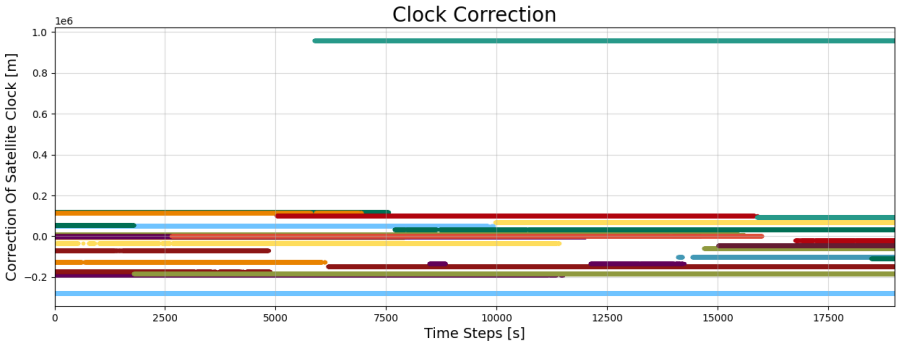

Figure 4.5: Clock Correction in meters for each time step.

Figure 4.6 depicts the correction of the tropospheric effect, $T^s = ZHD \cdot m_h^s + (ZWD_0 + \Delta ZWD) \cdot m_w^s$, for one satellite. It is rather stable for the first 15,000 time steps, with a correction between 2.5m to 5m. During the following 2,500 epochs, the correction increases slightly. The correction then decreases and finally reaches a value of about -5m. The correction is applied to the pseudorange and carrier phase measurements. Though the correction will differ for each satellite, they are generally not larger than 20m.

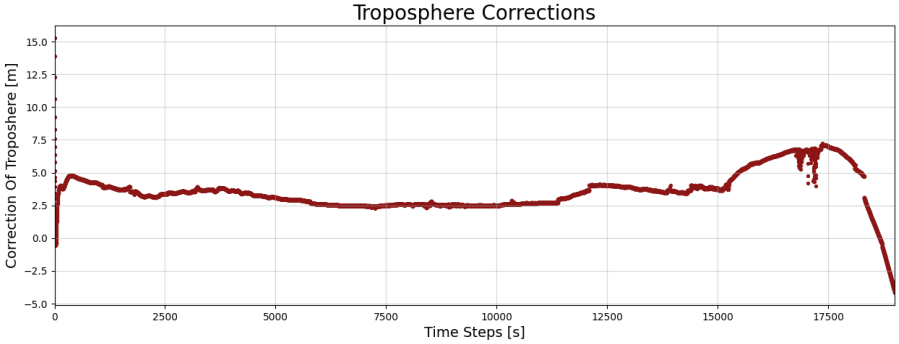

Figure 4.6: Troposphere correction for 19,000 time steps for one satellite.

The behaviour of the cycle slip detection for a satellite is shown in Figure 4.7. A vertical black line represents the time steps where a cycle slip is detected. The Figure also includes the true measurement $\mathbf{\Phi}_1 - \mathbf{\Phi}_5$ (blue) and predicted (red) measurements. The true and predicted measurements overlap for the first 12 time steps, and no cycle clips are detected. However, at the 13th epoch, a cycle slip occurs in the true measurement, causing an offset between the prediction and true measurement and a cycle slip is declared. Cycle slips are present until the true and predicted measurements overlap once again and overlap for at least 10 epochs.

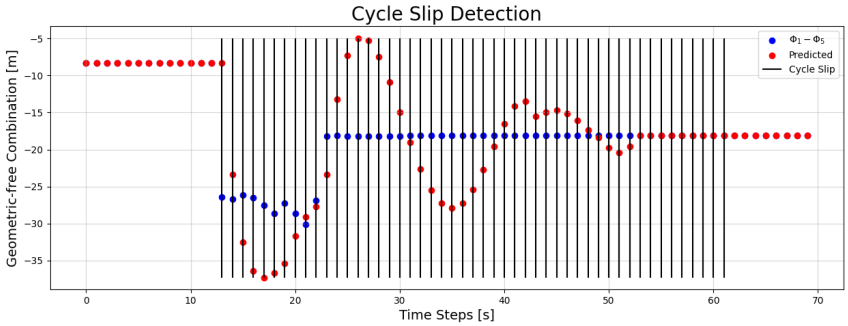

Figure 4.7: Detected cycle slips for 70 time steps for one satellite.

Figure 4.8 displays one satellite's antenna phase offset. This correction is applied to the satellite position before the position is interpolated to fit the data time steps. The precise product has 289 time steps with an available position to which the correction is applied. The correction has a ±1.5m magnitude in the x, y and z directions. The size, as well as the behaviour of the correction is similar for all satellites.

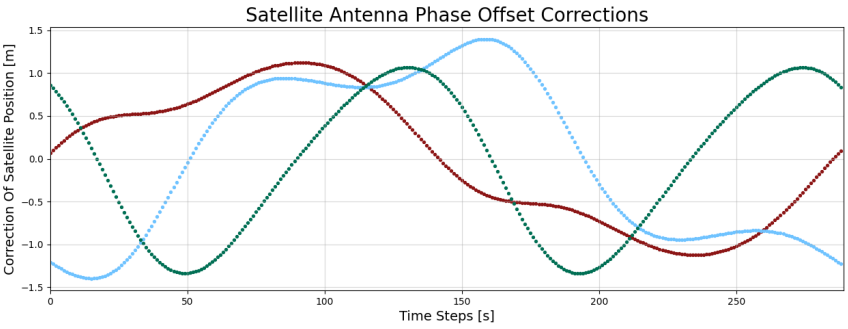

Figure 4.8: Antenna Phase Offset Correction in meters for the time steps available in the precise products for one satellite.

4.2 Dilution Of Precision

The expected accuracy of the observed data is shown as DOP graphs in Figures 4.9 and 4.10. Figure 4.9 depicts the horizontal DOP values for the first 19,000 epochs, and Figure 4.10 shows the corresponding vertical DOP values for the same data. An elevation angle cut-off is applied at 10° before calculating the DOP values to only include satellites that are used in the position estimation.

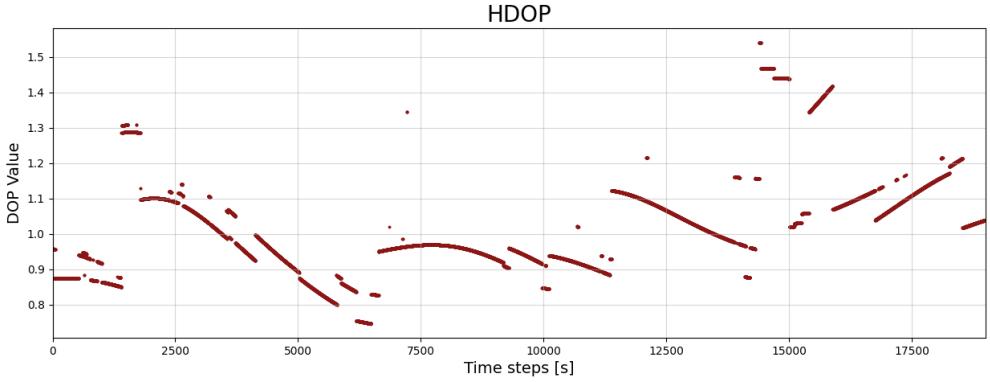

Figure 4.9: Horizontal DOP value for each time step using satellites with elevation angle larger than 10°.

As indicated by Figure 4.9, the horizontal DOP value is mostly between 0.7 and 1.2. Even the exceptions, the time steps where the HDOP exceeds a value of 1.3, are still close to 1. The outliers that do not follow the general graphs indicate a loss of connection to an important satellite.

The vertical DOP values presented in Figure 4.10 are similar in magnitude to those of the HDOP. All VDOP values are close to 1, within a range of 0.8 to 1.35. The values indicate low uncertainties for the data.

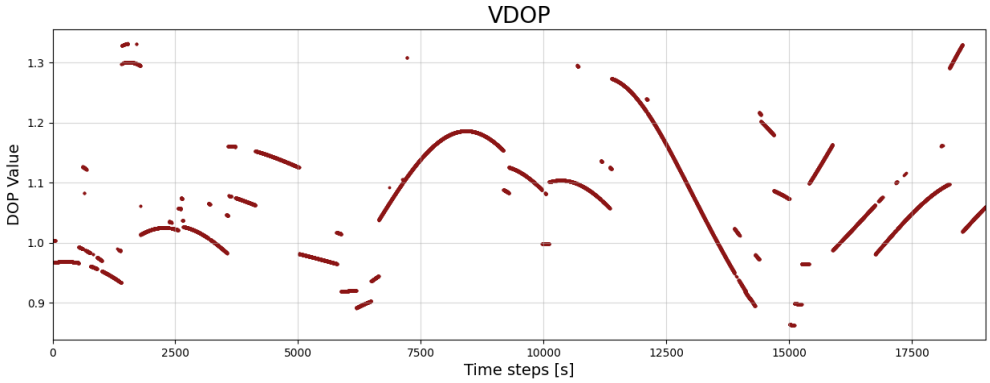

Figure 4.10: Vertical DOP value for each time step using satellites with elevation angle larger than 10°.

4.3 Number of Satellites

The number of visible satellites during the data capture is depicted in Figure 4.11, where the difference is shown between the amount of L1 capable satellites and L5 capable satellites. The number of L5 transmitting satellites is lower during the whole capture.

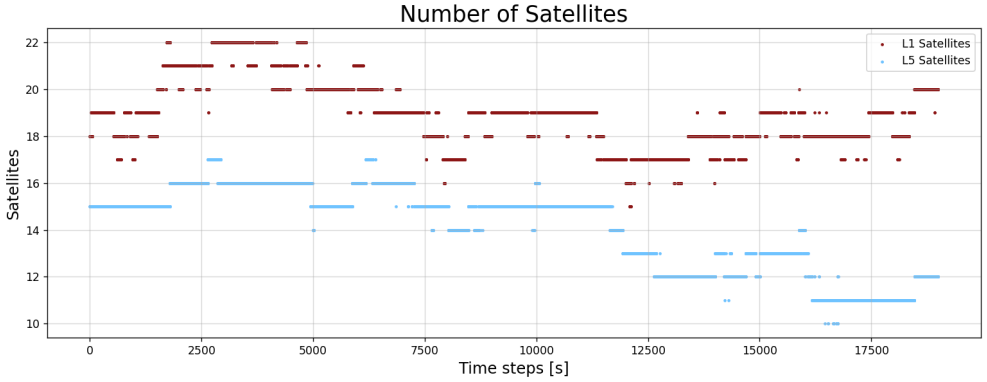

Figure 4.11: Number of satellites for the different frequency bands L1 and L5.

The number of satellites able to broadcast both the L1 and L5 frequencies with an elevation angle above 30° is depicted in Figure 4.12. It can be seen in the figure that the number of satellites with a higher elevation angle ($> 30°$) is at its lowest at around time step $11,000$ and highest at the start of the data capture.

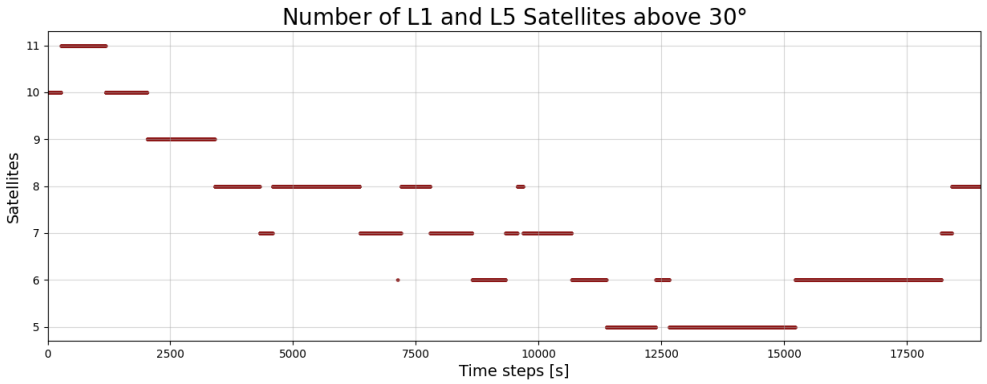

Figure 4.12: Number of satellites broadcasting L1 and L5 above 30° elevation angle.

Figure 4.13 displays the count of usable satellites, defined as those exceeding the elevation angle cut-off of 10°, free from cycle-slips and transmitting both L1 and L5 frequencies.

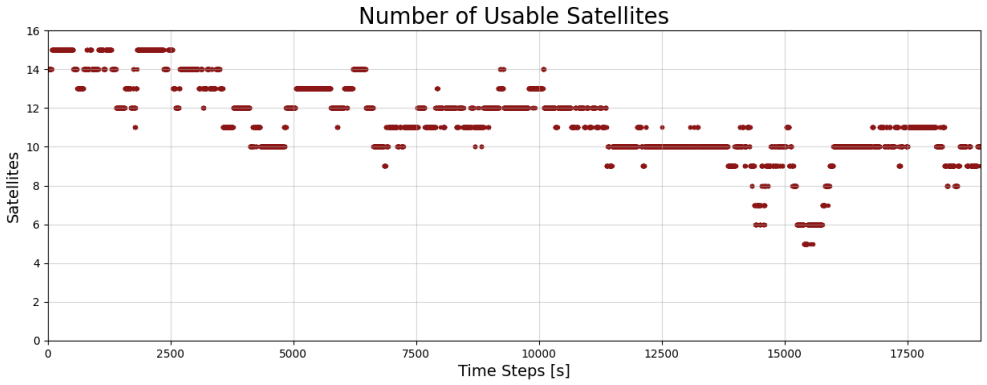

Figure 4.13: Number of usable satellites for the ionosphere-free combination of L1 and L5.

4.4 Vertical Accuracy

The vertical error refers to the accuracy of the height plane and is depicted in Figure 4.14. The Figure includes the true and estimated position. The graph showing the true position includes blue and red sections, which are indications of the state of the ambiguity. The graph is blue for epochs with float ambiguities and red when the ambiguities are fixed.

There is a large initial offset, off about 15m, before the estimation closes in on a 2m offset in the early epochs. The vertical accuracy is rather stable during epochs 4,000 to 11,000, averaging an offset of about 2.5m. After epoch 11,000, the accuracy decreases and is no longer stable.

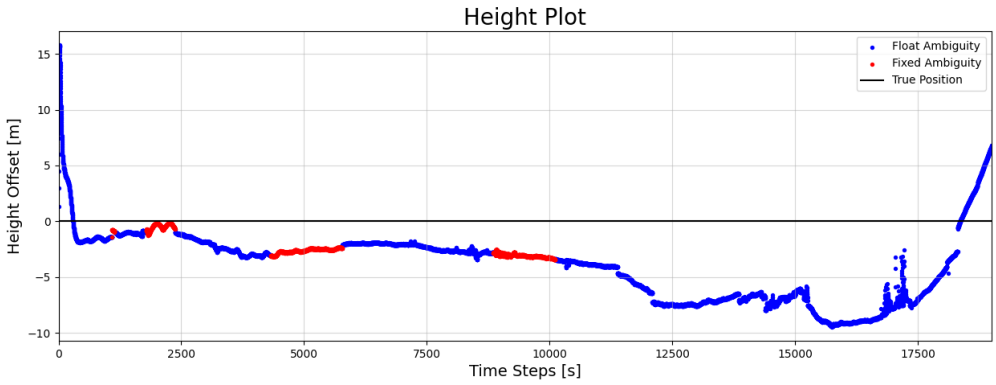

Figure 4.14: The offset in the height plane from the true position for 19,000 time steps.

4.5 Horizontal Accuracy

The horizontal accuracy, i.e. the accuracy in the East/West and North/South directions, is determined by analysing the distance between the estimated and the true position. The offset in the East/West direction is shown in Figure 4.15, and the North/South offset is depicted in Figure 4.16. As with the vertical accuracy, the colours of the graph for the estimated position indicate the state of the ambiguity for each epoch. The ambiguities are fixed during four periods, all happening before time step 11,000.

The offset in the East direction is stable and within decimetre-level during the first 11,000 epochs, with the exception of the large offset of the initial position. The accuracy is high until the second part of the data, the last 8,000 epochs. The estimated position starts to drift, and the accuracy decreases continuously.

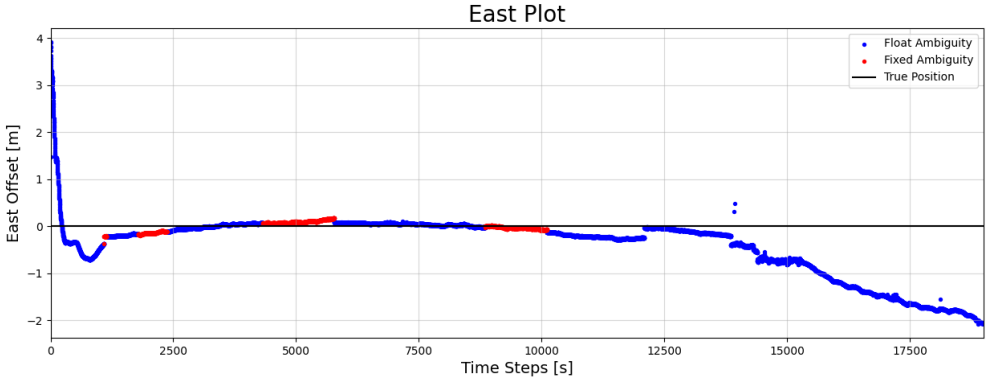

Figure 4.15: The offset in the East direction from the true position for 19,000 time steps.

Similar behaviours are visualised in the North direction in Figure 4.16, where the estimated position is stable until epoch 11,000. The initial uncertainty is present in this estimated position, but there is a fast recovery before converging to an offset of about 3m. As seen previously, the graph's behaviour changes at step 11,000.

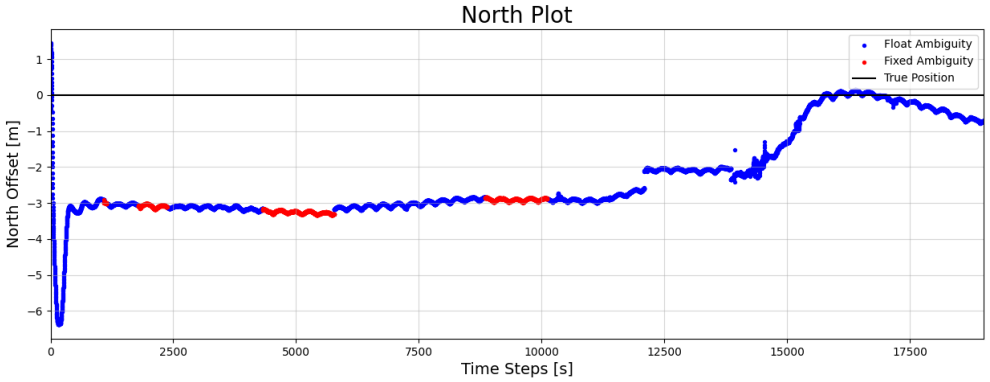

Figure 4.16: The offset in the North direction from the true position for 19,000 time steps.

The first 11,000 time steps for the East and North offsets are plotted in Figures 4.17 and 4.18 due to larger uncertainties after 11,000 time steps. The position is fairly stable in both these figures but not completely static.

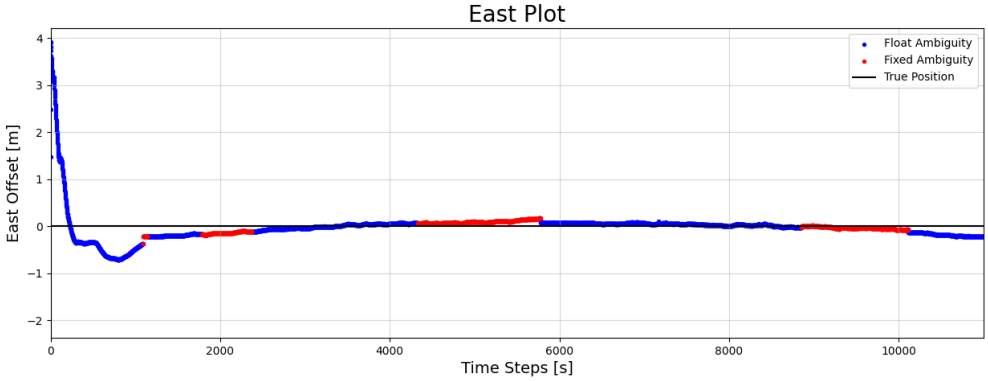

Figure 4.17: The offset in the East direction from the true position for 11,000 time steps.

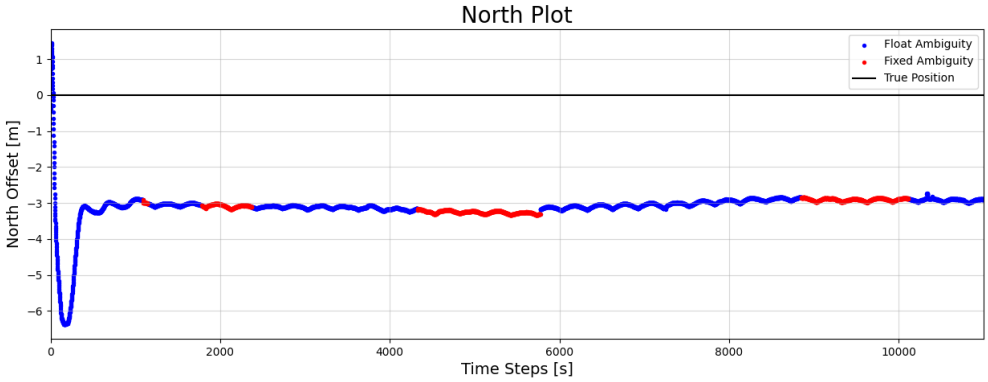

Figure 4.18: The offset in the North direction from the true position for 11,000 time steps.

4.6 RTKLIB Results

This section will show the results of using RTKLIB to process the collected data. In Figure 4.19, the East, North and altitude positions differ by tens of meters from the known position.

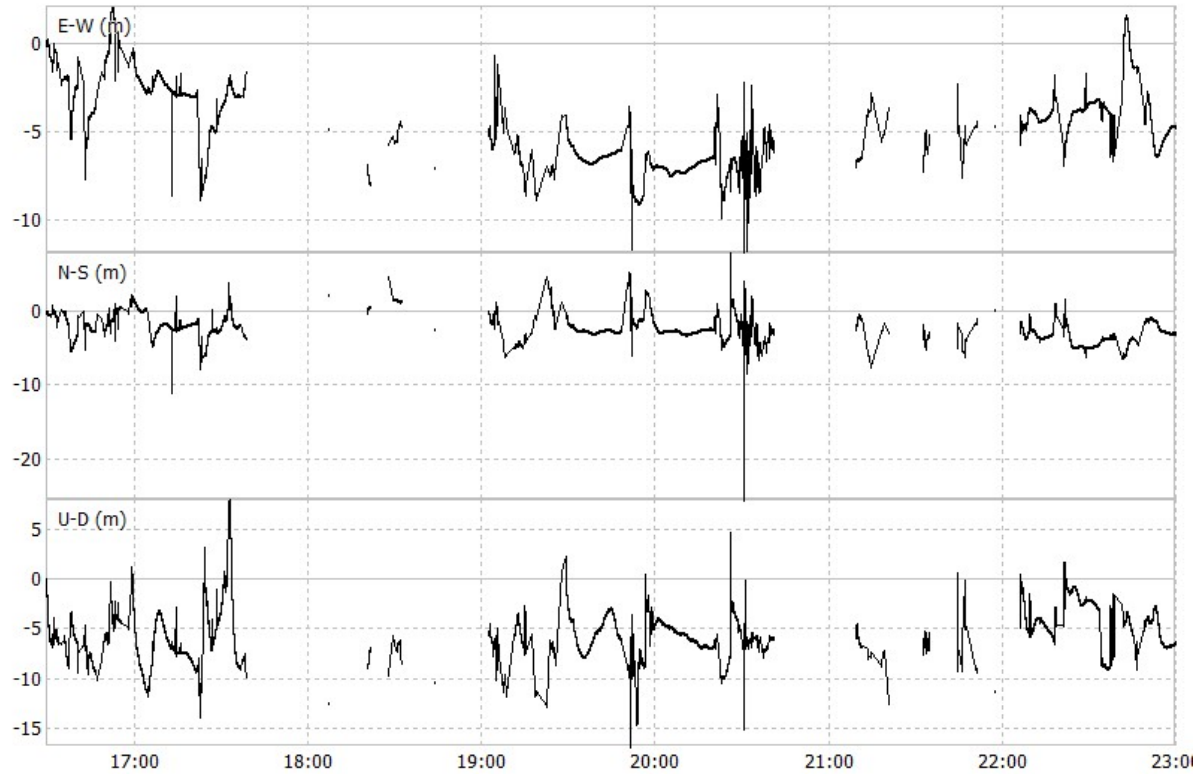

Figure 4.19: RTKLIB result in East, North and up directions, indicated by E-W, N-S and U-D respectively. The time in UTC is on the x-axis and the offset from the true position in each direction is shown on the y-axis.

In Figure 4.20, the number of usable satellites is shown. As can be seen, many of the time steps consist of ~ 5 usable satellites and some time steps, no usable satellites are detected.

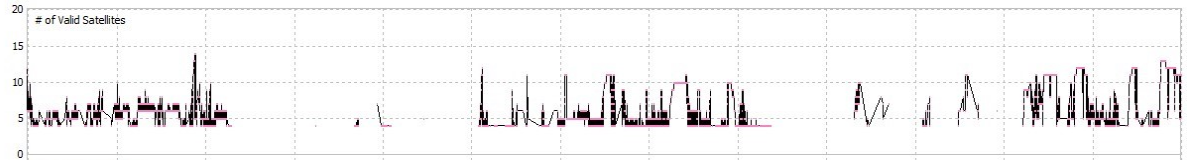

Figure 4.20: RTKLIB number of satellites.

5

Discussion

This section covers the attained accuracy of the implementation and the factors that influence it. Additionally, it includes explanations of how the results can be enhanced. The effects of the corrections, as well as their limitations, are discussed. The potential uncertainties of the collected data are also presented. Finally, the proposed future work is outlined.

5.1 Accuracy

The results presented in the previous chapter match the expectations of how well this solution would work at this stage. The most important result is the positional accuracy in the horizontal plane (North and East), which delivers decimetre-level accuracy when the ambiguities are fixed.

As noted, it is possible to see in Figures 4.16 and 4.15 that the positional accuracy severely degrades after $\sim 11,000$ time steps. The reason for this is not completely known, but most likely, it is related to the amount of visible and not cycle-slipped satellites. It can be seen in Figure 4.13 that the amount of usable satellites decreases during the data collection, and at its lowest, there are only five usable satellites, which is not enough to estimate a position correctly. The implemented EKF uses six states plus the ambiguity states. When the number of satellites is below six, and the ambiguities are not fixed, there are too many unknown variables compared to measurements, making the system underdetermined.

The displayed DOP values in Figures 4.9 and 4.10 suggest good outcomes for both vertical and horizontal positions throughout the entire sampling duration. Given the application's focus on horizontal accuracy, the HDOP takes importance. HDOP primarily relies on satellite azimuth angles rather than elevation angles, although the latter significantly impacts signal noise. Figure 4.12 shows a significant decrease in the number of satellites above 30° during data capture, particularly at time step 11,000. This reduction in high-elevation satellite availability may contribute to the degradation of the position estimate.

More constellations could be considered in the implementation to fix the issue of having too few usable satellites. Currently, only GPS and Galileo are considered for simplicity, but GLONASS and Beidou have operational satellites in the area. GLONASS however, does not transmit the L5 signal, making all of its satellites unusable for this work. Beidou transmits L5 on some of its satellites, but the amount in this area is low due to its main operation in China.

The most promising solution would be switching hardware that is able to receive and process the L1 and L2 signal combination. There are plenty of visible satellites, but not all of them transmit the L5 signal, making them unusable for this work. As can be seen in Figure 4.11, at the lowest, there are 15 visible satellites with L1 and only 10 for the L5 signal. Since all L1 frequency transmitting satellites can transmit the L2 frequency, the number of satellites would be much higher with that combination.

Before 11,000 seconds, the results look promising with decimetre precision in the horizontal plane as seen in Figures 4.17 and 4.18. Noteworthy is the offset in the north direction, discussed in Section 5.3 and the drift of the position even when the ambiguities are fixed, discussed in Section 5.2. Due to cycle slips, the longest period of fixed ambiguities is about $\sim$ 1500 seconds. Since a cycle slip usually happens for one satellite at a time, the position estimate remains roughly the same after the cycle slip. The rest of the ambiguities do not remain fixed but mostly keep the same value, most likely due to the estimated ambiguity being close to correct and, thus, not needing to be updated.

Compared to the solution from RTKLIB in Figure 4.19, the results from the implemented solution are very good. The same clock and orbit files were loaded into RTKLIB, and the kinematic mode was used to estimate the position. There are gaps in the estimated positions and number of satellites in the RTKLIB solution, this is most likely due to the low number of satellites, causing undetermined equations. The reason for the fewer satellites during the RTKLIB solution is not known.

5.2 Corrections

The Method Section 3.4 explains that corrections can be calculated either offline or online. This setup simplifies the implementation of the solution. By handling most error sources offline, the corrections for all time steps can be calculated before the position estimation starts. This process is less computationally complex, as the corrections are only applied in and not calculated within the Kalman filter. While the calculations of most offline corrections could be run in the filter, the implementation is still limited to post-processing because precise products are used for the clock and orbit corrections.

The results of the corrections, presented in Section 4.1, provide an indication of the magnitude of their impact on the solution accuracy. The corrections with large magnitudes, such as the earth rotation and clock correction, are especially important to implement as they greatly affect the estimation. The solid tides and satellite antenna phase offset are some corrections with a smaller magnitude, not exceeding 1m. However, for high-accuracy systems, smaller corrections matter.

Cycle slip detection has a great impact on system accuracy. If cycle slips are left untreated, the accuracy decreases. As cycle slips are changes in the number of wavelengths, detecting and handling them becomes especially important when performing ambiguity resolution.

Though the solution performs well for this data, some improvements regarding the corrections could be applied to improve the results further. One of them is the antenna phase offset. The current implementation determines the antenna phase offset corrections based on the L1 frequency, which is not comparable to the correction of the L5 frequency. The

reason for this is the lack of data for L5 APO due to the recentness of the L5 signal. This would also be fixed if the L1 and L2 combination were used.

The fixing of the ambiguities is dependent on removing the satellite hardware biases, $b^s_{WL,SD}$ and $b^s_{NL,SD}$, for the WL and NL measurements that are shown in Equations (3.19) and (3.20). The current implementation does not handle these biases, meaning the fixed solution is not completely free of biases causing a drift even if the ambiguities are fixed.

5.3 Data

As discussed in Section 3.5, the data for this project was gathered on the rooftop of a building in Mölndal. There was no precise marking of a position with high accuracy that could be used as a reference when evaluating the results of the estimated position. Instead, the longitude and latitude of the true position were determined using Google Maps. This method may introduce some uncertainties regarding the accuracy of the true position shown in Figures 4.14-4.16. Since the antenna's position was on top of a roof and the satellite picture on Google Maps is not taken straight above the building, an offset of the position will be introduced. Since the satellite picture is taken from the apparent south, it will introduce an offset in the north-south direction, visible in Figure 4.18.

5.4 Future Work

There are some areas in which this project can be improved with future work. New data should be collected at a location with a more accurate reference point to ensure that there are no constant bias offsets in the estimated position. Also, using new data to test the implementation would be beneficial as it enables validation of the system under other circumstances, such as different tropospheric conditions and satellite orbits. Many parameters can be tuned, and a more general model can be developed by testing multiple different kinds of data. It would also be possible to implement a RINEX parser so that data from various other sources could be tested. RINEX is a popular format for GNSS observations and is used as a standard for GNSS observation centres.

There are also error sources not considered in this implementation that need to be considered moving on. Biases like DCBs, described in Section 2.30, present in the pseudorange and carrier phase ionosphere-free combination, are not handled. Since the DCBs for the ionosphere-free combination of L1 and L2 are bundled with the precise clock product, it is hard to adapt to the L1 and L5 ionosphere-free combination and thus not handled. A work where this is handled for L1 and L5 ionosphere-free combination is cited here [48]. To correctly estimate the integer ambiguities, the phase hardware biases discussed in Section 5.2 must also be considered.

Running the system in real-time is a possible future improvement. The offline corrections should be calculated and applied in the Kalman filter at each epoch for the current time stamp to achieve this. Also, the precise orbit and clock products will have to be replaced. One possibility is developing a PPP-RTK based on the current PPP-AR solution by utilising SSR corrections, which are discussed in Section 2.6.2.3. The necessary steps to incorporate SSR corrections into the model are investing in another receiver that can

receive SSR corrections via L-band or ensuring that the receiver has internet access and can stream the SSR corrections via NTRIP. A change in the estimation process must also be performed as the current solution estimates the ambiguities of the ionosphere-free combination of L1 and L5. Better results have been achieved by using the ionosphere parameters provided in the SSR message, and thus, an estimation of the uncombined ambiguities is necessary [5][49][29].

6

Conclusion

The project demonstrated that high accuracy can be achieved cost-effectively using a low-cost receiver (EVK-F9P) capable of capturing both L1 and L5 signals. The hardware used is precise and inexpensive, with both receiver module and antenna included in the evaluation kit for a simple setup.

A working PPP model has been developed based on the data provided by the receiver. The solution includes multiple corrections of the error sources commonly disturbing GNSS. The corrections are of different magnitudes, and the most important ones to implement initially are the ones of large magnitudes. In the case of a high-accuracy solution, even the corrections of lower magnitude are essential. Offline corrections were applied to improve the accuracy of the position estimates. However, biases like DCBs and phase hardware biases remain areas for future improvement.

The implemented solution was compared to RTKLIB tool, using the same data, precise products and kinematic mode. While the current solution achieved decimeter-level accuracy when ambiguities were fixed, further enhancements are possible by incorporating real-time corrections (e.g., SSR) and improving ambiguity resolution.

Due to the time-consuming nature of testing, only a single scenario was tested with the described hardware. The test sites had to be in a location clearly visible on Google Maps so that close to exact coordinates could be retrieved. The location should also have few or no obstructions, such as tall buildings, to prevent multipath.

It is exciting to see that the L1/L5 combination can be used with PPP. The number of satellites is still too low to consistently determine a precise position, but good results will be possible in the future when more L5-compatible satellites are operational.

The implementation could become increasingly robust and accurate by improving the current solution and applying the suggested future work, such as real-time implementation and addressing remaining biases.

Bibliography

[1] Mike1024. *ECEF ENU Longitude Latitude relationships*. 2010. URL: https://commons.wikimedia.org/wiki/File:ECEF_ENU_Longitude_Latitude_relationships.svg.

[2] Bhamer. *Earth's atmosphere and ionosphere*. 2007. URL: https://en.m.wikipedia.org/wiki/File:Atmosphere_with_Ionosphere.svg.

[3] Elliott D. Kaplan and Christopher J. Hegarty. *Understanding GPS/GNSS: Principles and applications*. 3rd ed. Artech House, 2017. URL: https://ebookcentral.proquest.com/lib/chalmers/detail.action?docID=5430709#.

[4] J. Sanz Subirana, J.M Juan Zorzona, and M. Hernández-Pajares. *GNSS Data Processing*. Ed. by K.Editor Fletcher. ESA Communications, 2013. URL: https://gssc.esa.int/navipedia/GNSS_Book/ESA_GNSS-Book_TM-23_Vol_I.pdf.

[5] Xiangdong An, Ralf Ziebold, and Christoph Lass. "PPP-RTK with Rapid Convergence Based on SSR Corrections and Its Application in Transportation". In: *Remote Sensing* 15.19 (Jan. 2023), p. 4770. DOI: https://doi.org/10.3390/rs15194770. URL: https://www.mdpi.com/2072-4292/15/19/4770.

[6] "IEEE Standard Letter Designations for Radar-Frequency Bands". In: *IEEE Std 521-2019 (Revision of IEEE Std 521-2002)* (2020), pp. 1–15. DOI: 10.1109/IEEESTD.2020.8999849.

[7] Padma Bolla and Kai Borre. *Performance analysis of dual-frequency receiver using combinations of GPS L1, L5, and L2 Civil Signals*. July 2018. URL: https://link.springer.com/article/10.1007/s00190-018-1172-9#rightslink.

[8] John B. Anderson, Tor Aulin, and Carl-Erik Sundberg. "Chapter 1. Introduction". In: *Digital Phase Modulation*. 1st ed. Springer, 1986, pp. 1–14.

[9] Chris McAlister. "3.4 GNSS Signals". In: *usq.pressbooks.pub* (Sept. 2023). URL: https://usq.pressbooks.pub/gpsandgnss/chapter/3-4-gnss-signals/.

[10] Vincenzo Pesce, Pablo Hermosin, Aureliano Rivolta, et al. "Chapter Nine - Navigation". In: *Modern Spacecraft Guidance, Navigation, and Control*. Ed. by Vincenzo Pesce, Andrea Colagrossi, and Stefano Silvestrini. Elsevier, 2023, pp. 441–542. ISBN: 978-0-323-90916-7. DOI: https://doi.org/10.1016/B978-0-323-90916-7.00009-3. URL: https://www.sciencedirect.com/science/article/pii/B9780323909167000093.

[11] Cillan O´Driscoll Mark Petovello. "Carrier phase and its measurement for GNSS". In: *InsideGNSS* (2010), pp. 18–22.

[12] Vincenzo Pesce, Pablo Hermosin, Aureliano Rivolta, et al. "Chapter Nine - Navigation". In: *Modern Spacecraft Guidance, Navigation, and Control*. Ed. by Vincenzo Pesce, Andrea Colagrossi, and Stefano Silvestrini. Elsevier, 2023, pp. 441–542. ISBN: 978-0-323-90916-7. DOI: https://doi.org/10.1016/B978-0-323-

90916-7.00009-3. URL: https://www.sciencedirect.com/science/article/pii/B9780323909167000093.

[13] Guochang Xu. *GPS*. en. 2nd ed. Berlin, Germany: Springer, Aug. 2007.

[14] Dennis Odijk. "Ionosphere-Free Phase Combinations for Modernized GPS". In: *Journal of Surveying Engineering-asce - J SURV ENG-ASCE* 129 (Nov. 2003). DOI: 10.1061/(ASCE)0733-9453(2003)129:4(165).

[15] Jan Johansson. *Lecture 5 Atmospheric Effects*. 2022. URL: https://chalmers.instructure.com/courses/21151/files/folder/Lectures?preview=2431822.

[16] NovAtel Inc. *AN INTRODUCTION TO GNSS*. NovAtel Inc, 2023. ISBN: 978-0-9813754-1-0.

[17] Jan Van Sickle. *Welcome to GEOG 862: GPS and GNSS for Geospatial Professionals*. [Online; accessed 31-January-2024]. 2024. URL: https://www.e-education.psu.edu/geog862/node/1722.

[18] Martin Håkansson, Anna B. O. Jensen, Milan Horemuz, et al. *Review of code and phase biases in multi-gnss positioning - GPS solutions*. Oct. 2016. DOI: https://doi.org/10.1007/s10291-016-0572-7. URL: https://link.springer.com/article/10.1007/s10291-016-0572-7#citeas.

[19] International Earth Rotation and Reference Systems Services, Dennis D McCarthy, et al. *IERS conventions (2003)*. en. 2004.

[20] Abdelsatar Elmezayen and Ahmed El-Rabbany. "Real-time GNSS precise point positioning using improved robust adaptive Kalman filter". In: *Survey Review* 53.381 (2021), pp. 528–542. DOI: 10.1080/00396265.2020.1846361. eprint: https://doi.org/10.1080/00396265.2020.1846361. URL: https://doi.org/10.1080/00396265.2020.1846361.

[21] GMV. *Differential GNSS - Navipedia*. 2011. URL: https://gssc.esa.int/navipedia/index.php/Differential_GNSS.

[22] Manuel Hernández-Pajares et al. "Wide-area RTK". In: *Inside GNSS* (2010). URL: %5E1%5E.

[23] Thomas Grinter and Craig Roberts. *Real Time Precise Point Positioning: Are We There Yet?* 2013. URL: https://citeseerx.ist.psu.edu/document?repid=rep1&type=pdf&doi=0fc0f1263a54ed929f843ccaadbe7fe9c01f7c8b.

[24] J.F. Zumberge, M. Heflin, D.C. Jefferson, et al. "Precise Point Positioning for the Efficient And Robust Analysis of GPS Data from Large Networks". In: *Journal of Geophysical Research* 102 (Apr. 1997). DOI: 10.1029/96JB03860.

[25] Bofeng Li, Haibo Ge, Yuhang Bu, et al. "Comprehensive assessment of real-time precise products from IGS analysis centers". In: *Satellite Navigation* 3.1 (2022), p. 12. ISSN: 2662-1363. DOI: 10.1186/s43020-022-00074-2. URL: https://doi.org/10.1186/s43020-022-00074-2.

[26] Mohamed Elsheikh, Umar Iqbal, Aboelmagd Noureldin, et al. "The Implementation of Precise Point Positioning (PPP): A Comprehensive Review". In: *Sensors* 23.21 (2023). ISSN: 1424-8220. DOI: 10.3390/s23218874. URL: https://www.mdpi.com/1424-8220/23/21/8874.

[27] Oguz Kagan Isik et al. "Integrity Analysis for GPS-Based Navigation of UAVs in Urban Environment". In: *Robotics* 9.3 (2020). ISSN: 2218-6581. DOI: 10.3390/robotics9030066. URL: https://www.mdpi.com/2218-6581/9/3/66.

[28] u-blox. *EVK-F9P*. URL: https://www.u-blox.com/en/product/evk-f9p?legacy=Current#Product-description.

[29] Umberto Robustelli, Matteo Cutugno, and Giovanni Pugliano. "Low-Cost GNSS and PPP-RTK: Investigating the Capabilities of the u-blox ZED-F9P Module". In: *Sensors* 23.13 (2023). ISSN: 1424-8220. DOI: 10.3390/s23136074. URL: https://www.mdpi.com/1424-8220/23/13/6074.

[30] Roland Hohensinn, Raphael Stauffer, Marcus Franz Glaner, et al. "Low-Cost GNSS and Real-Time PPP: Assessing the Precision of the u-blox ZED-F9P for Kinematic Monitoring Applications". In: *Remote Sensing* 14.20 (2022). ISSN: 2072-4292. DOI: 10.3390/rs14205100. URL: https://www.mdpi.com/2072-4292/14/20/5100.

[31] Maxim Keshin, Yuki Sato, Kenji Nakakuki, et al. "A novel clock parameterization and its implications for precise point positioning and ionosphere estimation". en. In: *Sensors (Basel)* 22.9 (Apr. 2022), p. 3117.

[32] gps.gov. *New Civil Signals*. URL: https://www.gps.gov/systems/gps/modernization/civilsignals/.

[33] Eltehs SIA Company. *L1, L2, L5, L3, AND SIMPLY L FREQUENCY BANDS*. URL: https://gnss.store/blog/post/l1-l2-l5-l3-and-simply-l-frequency-bands.html.

[34] Lantmäteriet. *Galileo*. URL: https://www.lantmateriet.se/en/geodata/gps-geodesi-och-swepos/gps-and-satellite-positioning/gps-and-other-gnss/galileo/.

[35] NASA. *About the CDDIS GNSS data and products archive*. URL: https://cddis.nasa.gov/Data_and_Derived_Products/GNSS/GNSS_data_and_product_archive.html.

[36] NASA. *GNSS Orbit Products*. URL: https://cddis.nasa.gov/Data_and_Derived_Products/GNSS/orbit_products.html.

[37] NASA. *Station and Satellite Clock Products*. URL: https://cddis.nasa.gov/Data_and_Derived_Products/GNSS/clock_products.html.

[38] A. E. Niell. "Global mapping functions for the atmosphere delay at radio wavelengths". In: *Journal of Geophysical Research: Solid Earth* 101.B2 (Feb. 1996), pp. 3227–3246. DOI: 10.1029/95jb03048.

[39] John W. Marini. "Correction of satellite tracking data for an arbitrary tropospheric profile". In: *Radio Science* 7.2 (Feb. 1972), pp. 223–231. DOI: 10.1029/rs007i002p00223.

[40] J Sanz Subirana, J.M Juan Zornoza, and M Hernández-Pajares. *Tropospheric delay*. 2011. URL: https://gssc.esa.int/navipedia/index.php/Tropospheric_Delay.

[41] u-blox. *GNSS Raw Data*. 2023. URL: https://www.u-blox.com/en/technologies/gnss-raw-data.

[42] URL: https://swepos.lantmateriet.se/services/iono.aspx.

[43] Shuai Liu, Fuping Sun, Lundong Zhang, et al. "Tight integration of ambiguity-fixed PPP and INS: model description and initial results". In: *GPS Solutions* 20 (2015). DOI: 10.1007/s10291-015-0464-2.

[44] P. J. G. Teunissen. "The least-squares ambiguity decorrelation adjustment: a method for fast GPS integer ambiguity estimation". In: *Journal of Geodesy* 70.1 (Nov. 1995), pp. 65–82. ISSN: 1432-1394. DOI: 10.1007/BF00863419. URL: https://doi.org/10.1007/BF00863419.

[45] X.W. Chang, X. Yang, and T. Zhou. "MLAMBDA: a modified LAMBDA method for integer least-squares estimation". In: *Journal of Geodesy* (2005). DOI: 10.1007/s00190-005-0004-x.

[46] Marcus Glaner and Robert Weber. “PPP with integer ambiguity resolution for GPS and Galileo using satellite products from different analysis centers”. In: *GPS Solutions* 25.3 (May 2021). DOI: 10.1007/s10291-021-01140-z. URL: https://doi.org/10.1007/s10291-021-01140-z.

[47] T. Takasu. *RTKLIB ver. 2.4.2 Manual*. 2013. URL: http://www.rtklib.com/prog/manual_2.4.2.pdf.

[48] Qiong Wu, Mengfei Sun, Changjie Zhou, et al. “Precise Point Positioning Using Dual-Frequency GNSS Observations on Smartphone”. In: *Sensors* 19.9 (2019). ISSN: 1424-8220. DOI: 10.3390/s19092189. URL: https://www.mdpi.com/1424-8220/19/9/2189.

[49] Baocheng Zhang, Peter J.G. Teunissen, and Dennis Odijk. “A Novel Un-differenced PPP-RTK Concept”. In: *Journal of Navigation* 64.S1 (2011), S180–S191. DOI: 10.1017/S0373463311000361.

[50] J Sanz Subirana, J.M Juan Zornoza, and M Hernández-Pajares. *Mapping of Niell*. 2011. URL: https://gssc.esa.int/navipedia/index.php?title=Mapping_of_Niell.

A

Appendix 1

A.1 Transformation matrix from ECEF to ENU

$$R = \begin{bmatrix} -\sin\psi & -\sin\xi\cos\psi & \cos\xi\cos\psi \\ \cos\psi & -\sin\xi\sin\psi & \cos\xi\sin\psi \\ 0 & \cos\xi & \sin\xi \end{bmatrix} \tag{A.1}$$

Where

- ψ is the longitude of the receiver
- ξ is the latitude of the receiver.

A.2 Coefficients for hydrostatic and wet mapping functions

Table A.1: Rounded coefficients of the hydrostatic mapping function [50].

Coefficient ξ	**Latitude** (ϕ)				
	15°	30°	45°	60°	75°
	Average				
a	$1.277 \cdot 10^{-3}$	$1.268 \cdot 10^{-3}$	$1.247 \cdot 10^{-3}$	$1.220 \cdot 10^{-3}$	$1.205 \cdot 10^{-3}$
b	$2.915 \cdot 10^{-3}$	$2.915 \cdot 10^{-3}$	$2.929 \cdot 10^{-3}$	$2.902 \cdot 10^{-3}$	$2.902 \cdot 10^{-3}$
c	$62.61 \cdot 10^{-3}$	$62.84 \cdot 10^{-3}$	$63.72 \cdot 10^{-3}$	$63.82 \cdot 10^{-3}$	$64.26 \cdot 10^{-3}$
	Amplitude				
a	0	$1.271 \cdot 10^{-5}$	$2.652 \cdot 10^{-5}$	$3.400 \cdot 10^{-5}$	$4.120 \cdot 10^{-5}$
b	0	$2.141 \cdot 10^{-5}$	$3.016 \cdot 10^{-5}$	$7.256 \cdot 10^{-5}$	$11.72 \cdot 10^{-5}$
c	0	$9.013 \cdot 10^{-5}$	$4.35 \cdot 10^{-5}$	$84.80 \cdot 10^{-5}$	$170.4 \cdot 10^{-5}$
	Height Correction				
a_{ht}	$2.53 \cdot 10^{-5}$				
a_{ht}	$5.49 \cdot 10^{-3}$				
a_{ht}	$1.14 \cdot 10^{-3}$				

Table A.2: Rounded coefficients of the wet mapping function [50].

Coefficient ξ	**Latitude** (ϕ)				
	15°	30°	45°	60°	75°
a	$5.802 \cdot 10^{-4}$	$5.680 \cdot 10^{-4}$	$5.812 \cdot 10^{-4}$	$5.973 \cdot 10^{-4}$	$6.164 \cdot 10^{-4}$
b	$1.428 \cdot 10^{-3}$	$1.514 \cdot 10^{-3}$	$1.457 \cdot 10^{-3}$	$1.501 \cdot 10^{-3}$	$1.759 \cdot 10^{-3}$
c	$4.347 \cdot 10^{-2}$	$4.673 \cdot 10^{-2}$	$4,391 \cdot 10^{-2}$	$4.463 \cdot 10^{-2}$	$5.474 \cdot 10^{-2}$

A.3 Setup of EVK-F9P to send raw data

Inspired by this tutorial.

1. Download u-center here (ver. 23.08 is used in Windows 10)
2. Connect the receiver via USB to a computer and connect to the receiver in u-center with the correct port. Receiver → Connection
3. Wait until u-center starts displaying data in the plot windows (Might take up to several minutes)
4. In View → Messages:
   - Right-click on "NMEA" and "Disable Child Messages" which will disable NMEA and thus disable the plots in u-center.
   - From the "Messages" window, double click on "UBX" then "RXM". Right click and enable "RAWX" to enable raw observation messages and "SFRBX" to enable navigation messages.
5. In View → Gen 9 Configure
   - Select "GNSS Configuration", enable the desired constellations and signals, select "RAM" and "Flash" under "Layer Selection", then click on "Send Configuration".
6. In View → Configure:
   - Click on "RATE", and set "Measurement Period" to the desired time between observation samples, then click on "Send". This is set to 200ms.
   - Select "CFG", then "Save current configuration" then "Send" to save these settings to the flash on-board the F9P module.
7. In View → Packet Console:
   - If an antenna is connected to the receiver and is not completely blocked, verify that you see RAWX and SFRBX messages.

DEPARTMENT OF MECHANICS AND MARITIME SCIENCES
CHALMERS UNIVERSITY OF TECHNOLOGY
Gothenburg, Sweden 2024
www.chalmers.se

CHALMERS
UNIVERSITY OF TECHNOLOGY